Active nonlinear control of a stroke limited inertial actuator: theory and experiment

M. Dal Borgo[a,*], M. Ghandchi Tehrani[a], S.J. Elliott[a]

[a] *Institute of Sound and Vibration Research, University of Southampton, Southampton SO17 1BJ, Hampshire, UK*

Abstract

This paper presents a theoretical and experimental study of a stroke limited inertial actuator when used for active vibration control. The active control system under investigation consists of the inertial actuator attached to a flexible structure, a collocated vibration sensor and a velocity feedback controller (VFC). Controlling low frequency motions or large amplitude vibrations requires a very long stroke for the proof mass. However, a physical limitation of inertial actuators is that the stroke length is finite. Stroke saturation results in impulse-like excitation, which is transmitted to the structure and may result in damage. Additionally, these impacts between the proof mass and the end-stops can be in phase with the velocity of the structure, reducing the overall damping of the system, which leads to instability and limit cycle oscillations.

This paper examines the implementation of a nonlinear feedback controller (NLFC) to avoid collisions of the proof mass with the actuator's end-stops, thus preventing this instability. The nonlinear control strategy actively increases the internal damping of the actuator when the proof mass approaches the end-stops. The experimental implementation of the NLFC is investigated for the control of the first mode of a cantilever beam, and it is shown that the robustness of the VFC system to external perturbations is much improved with the NLFC. It is shown experimentally that larger velocity feedback gains can be used without

---

[*] Corresponding author

Email address: `m.dal-borgo@soton.ac.uk` (M. Dal Borgo)

the system becoming unstable when the NLFC is adopted and the theoretical reasons for this increase in stability margin are explored.

Keywords: Inertial actuator, stroke saturation, velocity feedback control, nonlinear feedback control

---

1. Introduction

Active vibration control plays a vital role in the attenuation of unwanted vibrations in lightweight and flexible structures, as recognised in a number of studies [1, 2, 3]. Velocity feedback controllers (VFCs) are a notable example of an active solution that can increase the effective damping of a structure, reducing its level of resonant vibration [4].

A VFC typically consists of an electromagnetic inertial, or proof mass, actuator attached to a structure, a collocated vibration sensor and a controller, which feeds back the velocity of the structure to the actuator. The aim of the inertial actuator is to apply a control force to the structure proportional to its velocity for the purpose of vibration reduction. The operating principle of an inertial actuator is that an input current to the actuator generates a control force on the structure by means of an electromagnetic transducer, reacting against a proof mass, which starts to accelerate [3]. An inertial actuator consists of a magnetic proof mass, an electrical winding and a suspension, which connects the proof mass to a casing or base mass. An example of such a device is shown in figure 1(a) and its schematic representation is displayed in figure 1(b).

Electromagnetic proof mass actuators have a wide range of applications. For example they can be used in: active vibration attenuation of space structures or satellites [6], active reduction of human induced vibration on floors of open-space buildings or on stadia [7], active or hybrid vibration control of skyscrapers swing induced by wind excitation [8], internal noise reduction in aircraft and active vibration isolation between the gearbox and the cabin of helicopters [9].

The internal dynamics of the inertial actuator is known to affect the stability and performance of the VFC, which then becomes only conditionally stable [10],

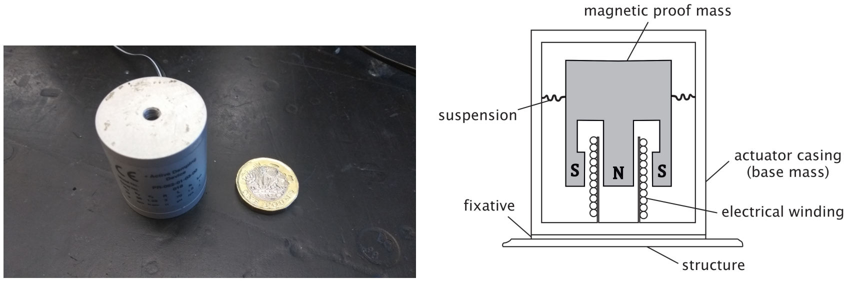

(a)

(b)

Figure 1: Electromagnetic inertial actuator. (a) Picture of a Micromega Dynamics IA-01 [5]; (b) Schematic of an inertial actuator in cross-section.

so that there exists a maximum velocity feedback gain, above which the control system becomes unstable [11]. Previous research has established that higher feedback gains are possible if the inertial actuator has a low natural frequency and a well damped resonance [11].

On the other hand, this solution increases the static displacement of the proof mass and its response to low frequency excitations. In practical applications, the maximum displacement of the proof mass is limited by the stroke length between the end-stops of the actuator [12]. For very low frequency motions or high input currents, the proof mass can saturate in stroke as it hits the end-stops, imparting large shocks to the structure, which may be damaged. Moreover, it has been observed both theoretically and experimentally that this nonlinear dynamic behaviour is also undesirable in terms of the stability of the closed-loop control system, because it can reduce the stability margin of the velocity feedback loop, and in fact, enhance the level of vibration [13, 14]. The instability is due to the forces imparted during the collisions between the proof mass and end-stops being in-phase with the velocity of the structure, hence reducing the overall damping of the system. Over-designing the actuator may not be possible in practice [12] and allowing for a very large stroke may negate the weight benefits introduced by these active devices.

This motivates an investigation into the causes and the effects of stroke saturation, and the development of a control strategy that can contrast the instability by increasing the range of stable control gains. The sources of mechanical and electromechanical nonlinearities in inertial actuators have been investigated in a previous study [15], where particular focus was given to stroke saturation.

Several attempts have been made to overcome the issue of stroke saturation in inertial actuators with the aid of active nonlinear control methods. The first study on this extent can be found in [16], where a suboptimal feedback position controller of a beam with a proof mass actuator was designed using a linear programming algorithm. This approach, however, severely limits the performance of the inertial actuator. Later studies developed the idea of adding a nonlinear feedback control loop to the VFC loop [17, 18, 19, 20, 21], but there is no record of experimental work using these controllers. Another approach that has been used is the on/off controller, which deactivates the VFC if stroke saturation is detected [22, 23]. A similar, but less dramatic strategy, namely gain scheduling, was first introduced by [24] and then adopted by [25, 26], where the VFC gain is reduced by a certain amount the more the proof mass gets close to the end-stops and eventually going to zero so that the system becomes passive. More recently, a double inner loop was proposed alongside the VFC, where one loop is a PD controller of the proof mass and the other loop adapts the velocity feedback gain depending on the value of the stroke [27]. A solution using linear methods, specifically a notch filter, was also discussed in [28].

This paper sets out a theoretical and experimental study of a nonlinear control strategy to prevent stroke saturation of inertial actuators, thus enhancing their stability when used with VFCs. The novel nonlinear feedback control (NLFC) strategy acts as a second feedback loop alongside the VFC and actively increases the internal damping of the actuator only when the proof mass gets closer to the end-stops. This is shown to increase the stability of the control system without affecting the performance.

This paper is organised in four main sections. Section 2 derives the mathematical model of the system constituted by a nonlinear inertial actuator attached to a SDoF structure controlled using a VFC loop. A theoretical investigation on the stability of the control loop is carried out comparing the nonlinear actuator model with the underlying linear one to show the importance of including the nonlinearity in the stability prediction. The NLFC law is then presented and analysed under different excitation conditions and a comparison between a single VFC loop or a combination of VFC and NLFC loops is carried out in terms of stability of the control system. Section 3 describes the experimental study conducted on a cantilever beam, where its second flexural mode is controlled by a stroke limited inertial actuator in direct velocity feedback. The experimental set-up is first presented. The NLFC developed in section 2 is then introduced as a second loop in the control strategy and the stability of the system is assessed comparing the cases when the nonlinear controller is implemented or not under different excitation conditions. The conclusions are summarised in section 4.

2. Nonlinear feedback control of a SDoF system: theoretical analysis

The nonlinear behaviour of inertial actuators described in [15] can be detrimental to the stability of VFCs, as observed in [13]. This section aims to develop a nonlinear strategy that accounts for the nonlinear dynamics of the actuator, enhancing the stability of the control system whilst maintaining the vibration attenuation performance provided by the VFC. A theoretical analysis of a stroke limited inertial actuator attached to a SDoF structure, driven by either a VFC or a combination of two feedback loops is presented. Firstly, the mathematical model of the nonlinear actuator, the structure and the feedback control system is derived in a state space form in section 2.1. Secondly, the stability of the closed-loop VFC system is addressed in section 2.2, comparing the results of the stability analysis of the underlying linear actuator model with the ones obtained from the nonlinear actuator model. The nonlinear feedback control (NLFC), which is a nonlinear function of the proof mass relative velocity and displacement, is presented in section 2.5. Finally, the results of numerical simulations showing the effectiveness of the proposed control law are discussed and compared with those of the VFC in terms of stability of the closed-loop system for different sets of feedback gains and primary excitation.

2.1. Mathematical model

Figure 2 shows a lumped parameter model of a SDoF system connected to a stroke limited inertial actuator, where the SDoF may represent the first mode of a real structure. Conventionally, all the displacements and forces pointing upwards are considered to be positive.

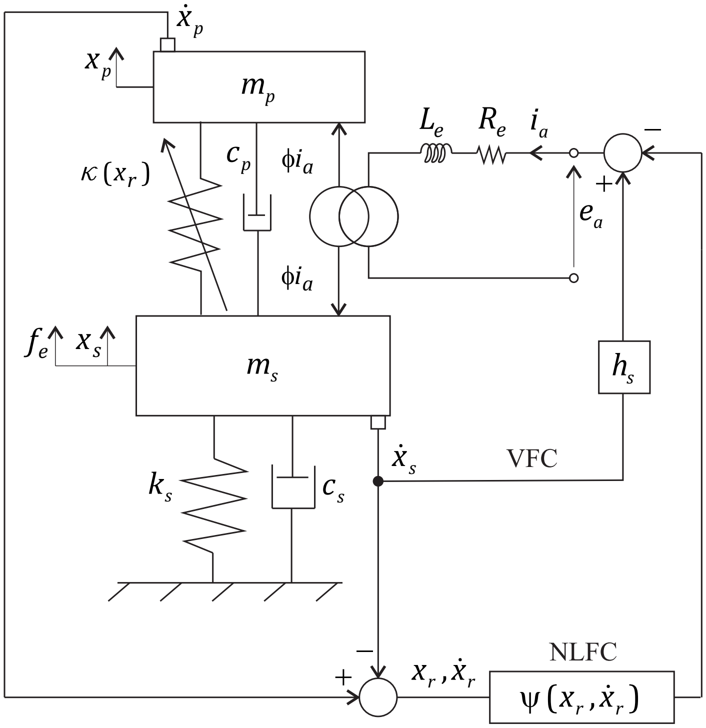

FIGURE 2: Lumped parameter model of the structure, nonlinear inertial actuator, velocity feedback controller (VFC) and nonlinear feedback controller (NLFC).

The proof mass and structural mass displacements are denoted as x_p and x_s , respectively. Also, $x_r = x_p - x_s$ represents the deflection of the proof mass from its resting position. The proof mass m_p is connected to the structural mass m_s via a damping coefficient c_p and a nonlinear stiffness that models the physics of stroke saturation [15], which is given by,

$$\kappa(x_r) = \begin{cases} k_p, & |x_r| < x_0 \\ k_p + k_c\left(1 - \frac{x_0}{x_r}\right), & |x_r| \geq x_0 \end{cases}, \tag{1}$$

where k_p is the underlying linear suspension stiffness, k_c is the end-stops stiffness and x_0 is the stroke length. The nonlinear restoring force given by $f_{RF}(x_r) = \kappa(x_r)x_r$ is also represented in figure 3 with the black solid line. The electrical winding of the actuator can be modelled as a series inductor L_e and resistor R_e and the voltage across the coil terminals is denoted as e_a. The structural mass is connected to the ground via the stiffness and damping parameters k_s and c_s, respectively. The structure is subject to the external, or primary, force $f_e(t)$ and the control, or secondary, force $\phi i_a(t)$ that is generated by the actuator transducer. The VFC loop is assumed to be implemented by scaling the structure's velocity $\dot{x}_s(t)$ by an arbitrary gain h_s and feeding this back to the actuator as the input current signal $i_a(t)$. A NLFC loop is added alongside the VFC loop in figure 2, and is defined as a nonlinear function of the relative

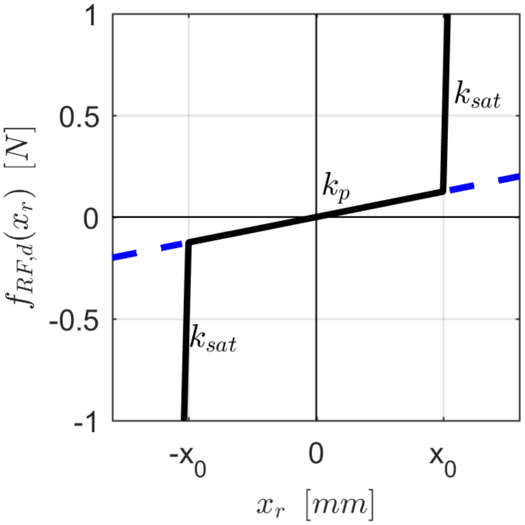

Figure 3: Restoring force for the underlying linear actuator (dashed line) and the stroke limited inertial actuator (solid line) .

proof mass velocity and displacement $\psi(x_r, \dot{x}_r)$. The equations of motion of the system in figure 2 can be expressed in a state space form as follows,

$$\begin{cases} \dot{\mathbf{x}}(t) = \mathbf{A}(\mathbf{x})\mathbf{x}(t) + \mathbf{B}_e f_e(t) + \mathbf{B}_a f_{a,s}(t) \\ \mathbf{y}(t) = \mathbf{C}\mathbf{x}(t) \end{cases}, \tag{2}$$

where $\mathbf{x}$ is the state vector defined as,

$$\mathbf{x} = \{ \begin{array}{cccc} x_s & x_p & \dot{x}_s & \dot{x}_p \end{array} \}^T, \tag{3}$$

and $\mathbf{A}(\mathbf{x})$ is the state dependent system matrix defined as,

$$\mathbf{A}(\mathbf{x}) = \begin{bmatrix} \mathbf{0} & \mathbf{I} \\ -\mathbf{m}^{-1}\mathbf{k}(\mathbf{x}) & -\mathbf{m}^{-1}\mathbf{c} \end{bmatrix}, \tag{4}$$

where $\mathbf{0}$ and $\mathbf{I}$ are the 2-by-2 null matrix and identity matrix, respectively. The mass matrix $\mathbf{m}$ can be written as,

$$\mathbf{m} = \begin{bmatrix} m_s & 0 \\ 0 & m_p \end{bmatrix}, \tag{5}$$

whereas the nonlinear stiffness matrix of the system $\mathbf{k}(\mathbf{x})$ appearing in eq.(4) results in,

$$\mathbf{k}(\mathbf{x}) = \begin{bmatrix} k_s + \kappa(\mathbf{x}) & -\kappa(\mathbf{x}) \\ -\kappa(\mathbf{x}) & \kappa(\mathbf{x}) \end{bmatrix}, \tag{6}$$

where $\kappa(\mathbf{x}) = \kappa(x_p - x_s)$ is given by eq.(1). Also, the system's damping matrix $\mathbf{c}$ is defined as,

$$\mathbf{c} = \begin{bmatrix} c_s + c_p & -c_p \\ -c_p & c_p \end{bmatrix}. \tag{7}$$

The input vector of the primary excitation can be written as,

$$\mathbf{B}_e = \{ \begin{array}{cccc} 0 & 0 & \frac{1}{m_s} & 0 \end{array} \}^T, \tag{8}$$

whereas the input vector of the secondary force is given by,

$$\mathbf{B}_a = \{ \begin{array}{cccc} 0 & 0 & \frac{1}{m_s} & -\frac{1}{m_p} \end{array} \}^T, \tag{9}$$

and the control force acting on the structure is

$$f_{a,s} = -\phi i_a. \tag{10}$$

The output vector is defined as,

$$\mathbf{y} = \{\ \dot{x}_s \quad \dot{x}_p\ \}^T, \tag{11}$$

hence, the output matrix can be written as,

$$\mathbf{C} = \{\ \mathbf{0} \quad \mathbf{I}\ \}, \tag{12}$$

where $\mathbf{0}$ and $\mathbf{I}$ are the 2-by-2 zero matrix and identity matrix. The state space eq.(2) can also be represented with the block diagram illustrated in figure 4, which also represents the open-loop control system since the input current is not directly related to the output variables. Hence, in general, the input current can be written as,

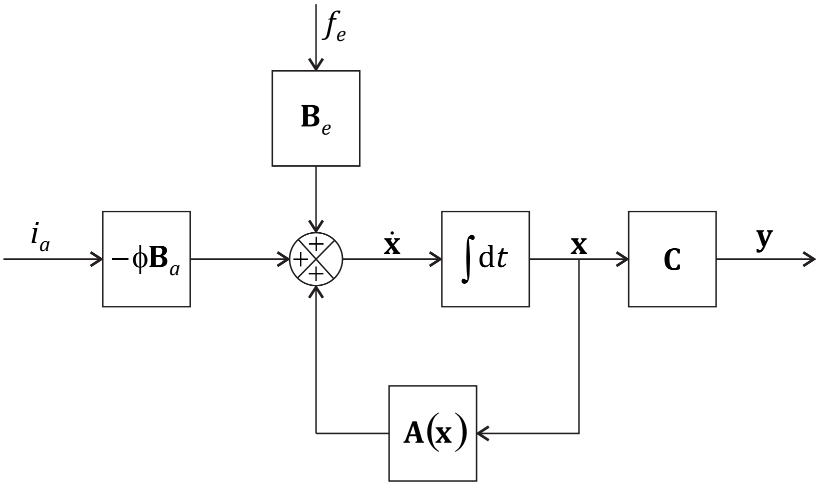

FIGURE 4: Block diagram of the open-loop system.

$$i_a = g_a \mathbf{H}\mathbf{r}, \tag{13}$$

where g_a is the amplifier gain, which is assumed to be unity throughout the paper, $\mathbf{r} = [r_1\ r_2]^T$ is the vector of reference signals and $\mathbf{H}$ is the matrix of control gains. The feedback control system, as shown in the schematic of figure 2 is made by closing the loop around the output vector, and hence imposing,

$$\mathbf{r} = \mathbf{y}. \tag{14}$$

Using eq.(14) and eq.(13), the input current of the feedback control system becomes,

$$i_a = g_a \mathbf{H}\mathbf{y}, \tag{15}$$

where $\mathbf{H}$ is the matrix of feedback control gains. For a single VFC loop on the structure's velocity, the matrix of feedback gains $\mathbf{H}$ can be rewritten as,

$$\mathbf{H}_{vfc} = \{\begin{array}{cc} h_s & 0 \end{array}\}, \tag{16}$$

hence, substituting eq.(16) into eq.(15), the driving current of the inertial actuator becomes,

$$i_{a,vfc} = g_a \mathbf{H}_{vfc}\mathbf{y} = \{\begin{array}{cc} h_s & 0 \end{array}\} \left\{ \begin{array}{c} \dot{x}_s \\ \dot{x}_p \end{array} \right\} = h_s \dot{x}_s. \tag{17}$$

For a single NLFC loop on the proof mass relative velocity, the matrix of feedback gains $\mathbf{H}$ can be rewritten as,

$$\mathbf{H}_{nlfc} = \{\begin{array}{cc} \eta_r(x_r) & -\eta_r(x_r) \end{array}\}, \tag{18}$$

where $\eta(x_r)$ is a nonlinear gain that depends on the proof mass relative position. Thus, substituting eq.(18) into eq.(15), the driving current of the inertial actuator becomes,

$$\begin{aligned} i_{a,nlfc} =& g_a \mathbf{H}_{nlfc}\mathbf{y} = \{\begin{array}{cc} \eta_r(x_r) & -\eta_r(x_r) \end{array}\} \left\{ \begin{array}{c} \dot{x}_s \\ \dot{x}_p \end{array} \right\} = \\ =& \eta_r(x_r)\dot{x}_s - \eta_r(x_r)\dot{x}_p = -\eta_r(x_r)\dot{x}_r = -\psi(x_r, \dot{x}_r). \end{aligned} \tag{19}$$

For a double feedback loop, hence, combining the VFC loop on the structure's velocity with the NLFC loop on the proof mass relative velocity, the matrix of feedback gains $\mathbf{H}$ becomes,

$$\mathbf{H}_{vfc+nlfc} = \{\begin{array}{cc} (h_s + \eta_r(x_r)) & -\eta_r(x_r) \end{array}\}. \tag{20}$$

The closed-loop control system block diagram of the state space eq.(2) is illustrated in figure 5, where the driving current is given by the combination of both the VFC and the NLFC loops defined by eq.(17) and eq.(19), respectively.

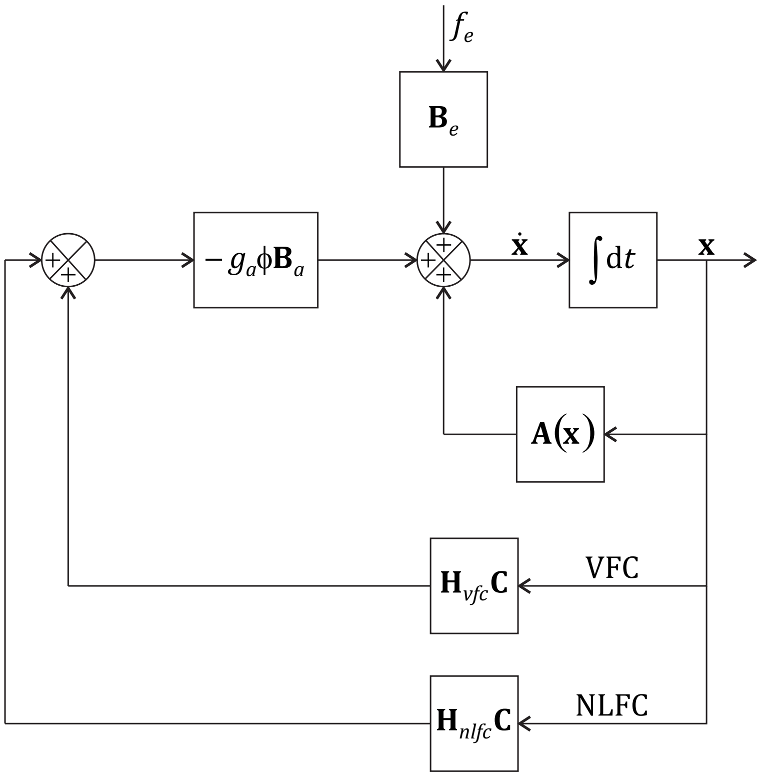

FIGURE 5: Block diagram of the closed-loop control system with both the VFC loop and the NLFC loop.

Considering a general matrix of feedback gains $\mathbf{H}$, the control force applied to the structure by the closed-loop system can be written by substituting eq.(15) into eq.(10). That is,

$$f_{a,s} = -\phi g_a \mathbf{H}\mathbf{y} = -g_a \phi \mathbf{H}\mathbf{C}\mathbf{x}, \tag{21}$$

hence, the state eq.(2) can be rewritten as,

$$\dot{\mathbf{x}}(t) = \mathbf{A}_0(\mathbf{x})\mathbf{x} + \mathbf{B}_e f_e(t), \tag{22}$$

where the closed-loop state dependent system matrix $\mathbf{A}_0(\mathbf{x})$ is derived as follows,

$$\mathbf{A}_0(\mathbf{x}) = \left[\mathbf{A}(\mathbf{x}) - g_a \phi \mathbf{B}_a \mathbf{H}\mathbf{C}\right]. \tag{23}$$

The parameters used in the numerical analysis of the system shown in figure 2 are provided in table 1. The natural frequencies and the damping ratios of the structure and actuator are also reported and have been calculated as $\omega = \sqrt{k/m}$ and $\zeta = c/2\sqrt{km}$, respectively. The system is also characterised by the ratio of the natural frequencies of the actuator and structure $\Omega = \omega_p/\omega_s$, which is small compared to unity for good linear performance, and the ratio of the nonlinear to the linear stiffness of the actuator, $K = k_c/k_p$, which is much greater than unity.

2.2. Absolute velocity feedback control

VFCs, in which the velocity of the structure is fed back to a collocated inertial actuator are only conditionally stable [11], hence, there exists a maximum feedback gain, over which the system becomes unstable, due to inclusion of the actuator dynamics. Moreover, if the external excitation or the feedback gain is such that the inertial actuator saturates in stroke, then the control system may become unstable for even lower control gains than those predicted by a liner stability analysis [14, 13]. In this section the stability of the VFC is first assessed for the underlying linear system and secondly for the nonlinear system, when stroke saturation is taken into account.

2.3. Stability analysis and control performance for a linear actuator

The underlying linear model of the system in figure 2 is obtained by imposing a zero impact stiffness ($k_c = 0$), thus, the state dependent system matrix $\mathbf{A}(\mathbf{x})$ of eq.(4) becomes a constant state matrix

$$\bar{\mathbf{A}} = \mathbf{A}(\mathbf{x})\Big|_{k_c=0} \begin{bmatrix} \mathbf{0} & \mathbf{I} \\ -\mathbf{m}^{-1}\bar{\mathbf{k}} & -\mathbf{m}^{-1}\mathbf{c} \end{bmatrix}, \tag{24}$$

where the state dependent stiffness matrix $\mathbf{k}(\mathbf{x})$ given by 6 results in,

$$\bar{\mathbf{k}} = \mathbf{k}(\mathbf{x})\Big|_{k_c=0} \begin{bmatrix} k_s + k_p & -k_p \\ -k_p & k_p \end{bmatrix}, \tag{25}$$

TABLE 1: Table of model parameters.

Parameters	Value	Units
m_s	0.050	kg
k_s	5000	N/m
c_s	0.32	$\mathrm{N/ms^{-1}}$
m_p	0.031	kg
k_p	100	N/m
k_c	$2 \cdot 10^4$	N/m
c_p	1.4	$\mathrm{N/ms^{-1}}$
x_0	1.25	mm
ϕ	1.55	N/A
g_a	1	$\mathrm{A/ms^{-1}}$
System Characteristics	**Value**	**Units**
ω_p (actuator)	$2\pi 9.7$	rad/s
ω_s (structure)	$2\pi 50.3$	rad/s
Dimensionless Parameters	**Value**	**Units**
ζ_p (actuator)	39	%
ζ_s (structure)	1	%
$\Omega = \frac{\omega_p}{\omega_s}$	0.2	-
$K = \frac{k_c}{k_p}$	200	-

hence, the closed-loop state dependent system matrix $\mathbf{A}_0$ becomes,

$$\bar{\mathbf{A}}_0 = \left[\bar{\mathbf{A}} - g_a \phi \mathbf{B}_a \bar{\mathbf{H}} \mathbf{C}\right]. \tag{26}$$

where $\bar{\mathbf{H}} = [h_1 \; h_2]$ is a matrix of constant gains, which means that only linear feedback loops are considered. If the underlying linear system is driven by the VFC loop only, the output eq.(2) becomes,

$$y = \mathbf{C}_{vfc}\mathbf{x} = \dot{x}_s, \tag{27}$$

where the output matrix $\mathbf{C}_{vfc}$ is defined as,

$$\mathbf{C}_{vfc} = \begin{bmatrix} 0 & 0 & 1 & 0 \end{bmatrix}. \tag{28}$$

Setting $f_e = 0$ and assuming zero initial conditions $\mathbf{x}(0) = 0$, the Laplace transform of the the state eq.(2) for the underlying linear system becomes,

$$\mathbf{X}(s) = \left[s\mathbf{I} - \bar{\mathbf{A}}\right]^{-1} \mathbf{B}_a F_{a,s}(s), \tag{29}$$

substituting the Laplace transform of eq.(10) into eq.(29) results in,

$$\mathbf{X}(s) = -\phi \left[s\mathbf{I} - \bar{\mathbf{A}}\right]^{-1} \mathbf{B}_a I_a(s), \tag{30}$$

and substituting eq.(30) into the Laplace transform of the output eq.(27) gives,

$$Y(s) = -\phi \mathbf{C}_{vfc} \left[s\mathbf{I} - \bar{\mathbf{A}}\right]^{-1} \mathbf{B}_a I_a(s). \tag{31}$$

Dividing eq.(31) by $-I_a(s)$ gives the plant transfer function $G_{sa}(s)$ as,

$$G_{sa}(s) = -\frac{Y(s)}{I_a(s)} = \phi \mathbf{C}_{vfc} \left[s\mathbf{I} - \bar{\mathbf{A}}\right]^{-1} \mathbf{B}_a. \tag{32}$$

In general, the input current can be written as,

$$I_a(s) = g_a h_s r(s), \tag{33}$$

where $r(s)$ is a reference signal. Substituting eq.(33) into eq.(32) gives the open-loop transfer function $L(s)$ as,

$$L(s) = g_a G_{sa}(s) h_s, \tag{34}$$

which is also illustrated in the block diagram of figure 6.

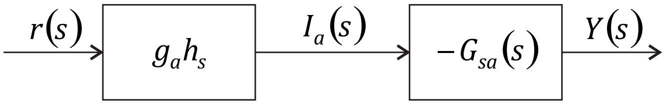

FIGURE 6: Block diagram of the open-loop VFC system.

Considering now the forced response, hence setting $f_e \neq 0$ and zero initial conditions $\mathbf{x}(0) = \mathbf{0}$, the Laplace transform of the state eq.(2) for the underlying linear system becomes,

$$\mathbf{X}(s) = \left[s\mathbf{I} - \bar{\mathbf{A}}\right]^{-1} \mathbf{B}_a F_{a,s}(s) + \left[s\mathbf{I} - \bar{\mathbf{A}}\right]^{-1} \mathbf{B}_e F_e(s). \tag{35}$$

Substituting eq.(35) into the Laplace transform of the output eq.(27) and considering eq.(10) gives,

$$Y(s) = -\phi \mathbf{C}_{vfc} \left[s\mathbf{I} - \bar{\mathbf{A}}\right]^{-1} \mathbf{B}_a I_a(s) + \mathbf{C}_{vfc} \left[s\mathbf{I} - \bar{\mathbf{A}}\right]^{-1} \mathbf{B}_e F_e(s), \tag{36}$$

which can be rewritten as,

$$Y(s) = -G_{sa}(s) I_a(s) + G_{se}(s) F_e(s), \tag{37}$$

where $G_{sa}(s)$ is given by eq.(32) and $G_{se}(s)$ is defined as follows,

$$G_{se}(s) = \mathbf{C}_{vfc} \left[s\mathbf{I} - \bar{\mathbf{A}}\right]^{-1} \mathbf{B}_e. \tag{38}$$

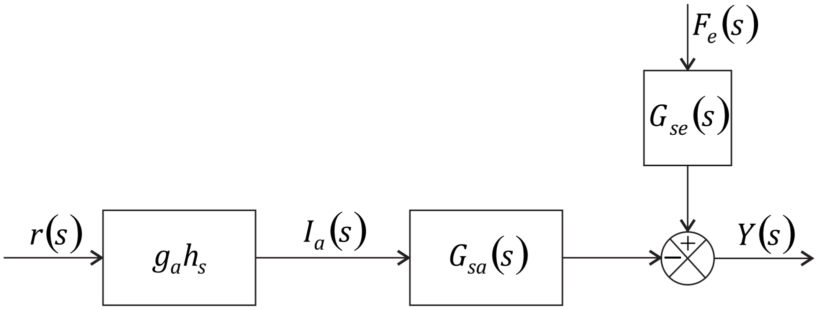

Figure 7: Block diagram of the open-loop VFC system including the disturbance of the external excitation.

The open-loop output eq.(37) that includes the disturbance given by the primary excitation is also displayed in figure 7. The closed-loop system is obtained by using the output signal as the reference signal, as shown in the block diagram of figure 8. The output equation of the closed-loop system can be written by substituting eq.(34) and eq.(33) into eq.(37) and imposing $r(s) = Y(s)$, which results in,

$$Y(s) = -L(s)Y(s) + G_{se}(s)F_e(s), \tag{39}$$

so that,

$$Y(s)(1+L(s)) = G_{se}(s)F_e(s), \tag{40}$$

and dividing eq.(40) by $F_e(s)$ gives the closed-loop transfer function $T(s)$ between the output velocity of the structure and the input disturbance to the system as,

$$T(s) = \frac{Y(s)}{F_e(s)} = \frac{G_{se}(s)}{(1+L(s))}, \tag{41}$$

which is defined for

$$1 + L(s) \neq 0. \tag{42}$$

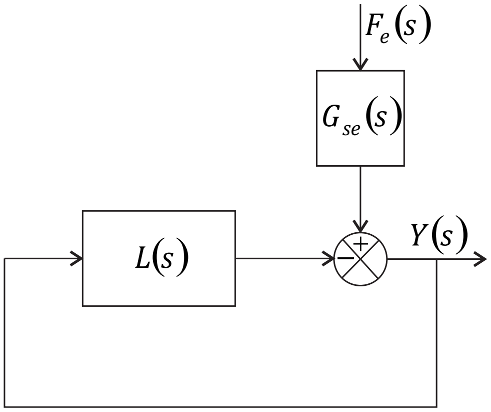

Figure 8: Block diagram of the closed-loop VFC system.

The stability of the closed-loop VFC for the underlying linear system can be studied using the Nyquist criterion. The Nyquist plot of the open-loop FRF $L(j\omega)$ given by eq.(34) for a velocity feedback gain $h_s = 21$ is shown in figure 9. The closed-loop VFC system is only conditionally stable as the polar plot crosses the real negative axis and a finite increase in gain would result in $L(j\omega)$ encircling the (-1,0) point.

The gain margin is given by,

$$g_m = \frac{1}{L(\omega_c)}, \tag{43}$$

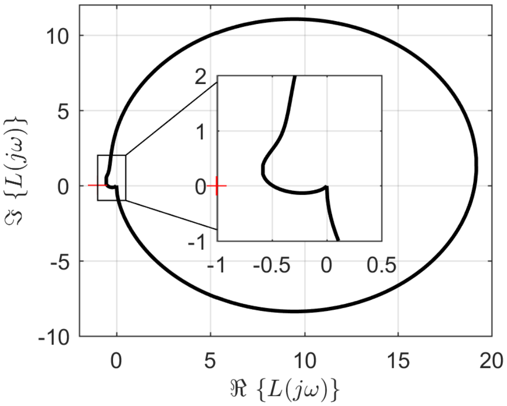

FIGURE 9: Nyquist plot of the open-loop FRF $L(j\omega)$ for a velocity feedback $h_s = 21$.

where $L(\omega_c)$ is the crossing point with the negative real axis and ω_c is the crossing frequency. For this system, the maximum feedback gain that can be used without causing instability ($g_m < 1$) is $h_{s,max} = 42$. The frequency of the crossing point in the Nyquist plot of figure 9, in which the system becomes unstable is $\omega_c = 2\pi 10$ rad/s, which is about the natural frequency of the inertial actuator.

2.4. Stability analysis for a nonlinear actuator

In this section the nonlinear dynamic behaviour of the inertial actuator due to the limited stroke is taken into account when evaluating the stability of the VFC. By introducing the actuator nonlinearity, the stability of the closed-loop VFC becomes dependent on both the relative proof mass displacement and the velocity feedback gains. This dependency can be analysed through the Lyapunov linearisation stability method [29, 30].

Lyapunov indirect and direct method are often used to asses the local and global stability of a nonlinear system, respectively [29]. The indirect method analyses the local stability of a nonlinear system around its equilibrium points by evaluating the eigenvalues of the Jacobian matrix of the nonlinear state space equation. If the real part of the eigenvalues is negative for all eigenvalues, then the system is locally stable. Vice-versa, if the real part of the eigenvalues is positive for any eigenvalue, then the system is locally unstable. The main drawback of this method is that it gives information only about the local stability. Lyapunov direct method, instead, analyses the global stability of a nonlinear system by searching an energy-like function of the states that satisfies a set of conditions [29]. However, it is usually difficult to find a suitable Lyapunov function that satisfies all the conditions. Additionally, it is even more difficult to demonstrate instability, because the non-existence of suitable Lyapunov functions has to be proved. An interesting analysis is given by the Lyapunov exponents of the nonlinear system, which allows to investigate the behaviour of the system around the initial condition $\tilde{\mathbf{x}}$ [30]. This case is similar to the direct method of Lyapunov, but the Jacobian matrix of the nonlinear state space equation is calculated at the initial condition $\tilde{\mathbf{x}}$ instead of the equilibrium point. If the eigenvalues of the Jacobian matrix have negative real part, then the nonlinear system is locally stable, if, instead, the eigenvalues of the Jacobian matrix have positive real part, then the nonlinear system is locally unstable [30].

The Jacobian matrix of the nonlinear state space equation is given by eq.(23). The VFC closed-loop state dependent system matrix can be derived from eq.(23) as,

$$\mathbf{A}_{0,vfc}(\mathbf{x}) = \left[\mathbf{A}(\mathbf{x}) - g_a \phi \mathbf{B}_a \mathbf{H}_{vfc} \mathbf{C}\right]. \tag{44}$$

and the stability of the closed-loop VFC system can be studied using the Lyapunov linearisation method, or Lyapunov exponent method, by calculating eigenvalues of eq.(44) for several proof mass relative displacements. If the real part of the largest eigenvalue is lower than zero, the system is stable, vice-versa if is greater than zero, then the system is unstable. The real part of the maximum eigenvalue of $\mathbf{A}_{0,vfc}$ for several proof mass displacements and velocity feedback gains is displayed in figure 10(a) and a detailed image around the stroke limit region is shown in figure 10(b), where the stroke limits are represented with dashed red lines. Figure 10 shows that the nonlinear system is stable for displacements within the stroke limits and feedback gains below $h_{s,max}$, as

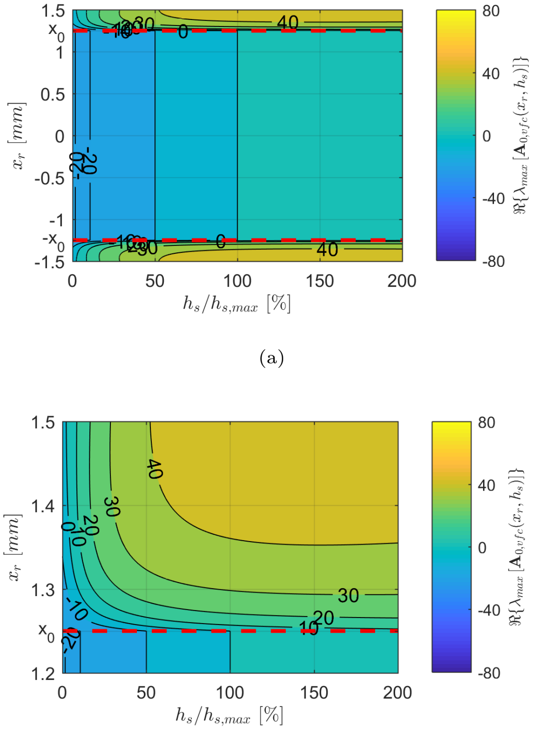

(a)

(b)

FIGURE 10: Real part of the maximum eigenvalue of the closed-loop matrix $\mathbf{A}_{0,vfc}(\mathbf{x})$ for several values of the relative proof mass displacement x_r and velocity feedback gain h_s. (a) full range; (b) zoom into the stroke limit.

expected. Also, the system becomes unstable for $h_s > h_{s,max}$ regardless of the relative displacement. The delimiter of instability $\Re\{\lambda_{max}\,[\mathbf{A}_{0,vfc}(x_r, h_s)]\} = 0$ shows that for a particular feedback gain $h_s < h_{s,max}$ there exists a relative displacement $|x_r| > x_0$ above which the system becomes unstable, and the higher is the feedback gain, the lower is the relative displacement required to make the system unstable.

The stability of the nonlinear system of figure 2 subject to a single VFC loop can also be evaluated using the describing function method [29, 31]. The nonlinear system can be represented using a feedback connection with the nonlinear element, as shown in figure 11, where $K_{eq}(X_r)$ is the describing function of the nonlinearity and $G(j\omega)$ groups the underlying liner dynamic behaviour of the system including also the VFC loop. The characteristic equation of the system in figure 11 is,

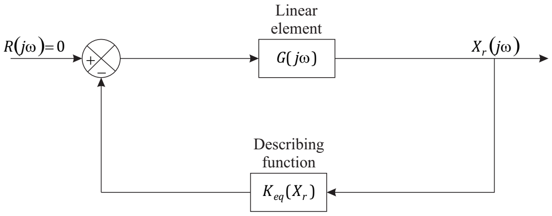

FIGURE 11: Block diagram of the describing function analysis for the existence of limit cycles.

$$G(j\omega)K_{eq}(X_r) + 1 = 0, \tag{45}$$

which can be rewritten as,

$$G(j\omega) = -\frac{1}{K_{eq}(X_r)}, \tag{46}$$

where the describing function $K_{eq}(X_r)$ is given by [15],

$$K_{eq}(X_r) = k_p + \frac{k_c}{\pi}\left[\pi - 2\arcsin\left(\frac{x_0}{X_r}\right) - 2\frac{x_0}{X_r^2}\sqrt{X_r^2 - x_0^2}\right], \tag{47}$$

and the linear FRF $G(j\omega)$ is given by,

$$G(j\omega) = \mathbf{C}_{DF}\left[s\mathbf{I} - \bar{\mathbf{A}}_{0,vfc}\right]^{-1}\mathbf{B}_a, \tag{48}$$

where the output matrix is defined as,

$$\mathbf{C}_{DF} = \left[\begin{array}{cccc} -1 & 1 & 0 & 0 \end{array}\right], \tag{49}$$

and the state matrix as,

$$\bar{\mathbf{A}}_{0,vfc} = \bar{\mathbf{A}} - g_a\phi\mathbf{B}_a h_s\mathbf{C}_{vfc}. \tag{50}$$

Figure 12 shows the polar plot of $G(j\omega)$ with the solid black line for a feedback gain $h_s = 75\% h_{s,max}$ and the loci of the describing function term with the dash-dotted red line. Since the nonlinearity considered here is an odd function, its describing function takes only real values, hence the term $-1/K_{eq}(X_r)$ lies on the negative real axis. It should be noted that this term starts from $-1/k_p$ for $|X_r| < x_0$, then it goes towards the origin as $|X_r|$ increases. The intersection between the polar plot with the negative inverse of the describing function, hence the solution of eq.(46), gives the condition for the existence of limit cycles in the nonlinear system [29, 31]. The amplitude of the limit cycle is given by the value of X_r corresponding to the negative inverse of the describing function at the point of intersection. Similarly, the frequency of the limit cycle ω_{lc} corresponds to the value of the frequency of the polar plot at the point of intersection. This procedure only gives a prediction of the existence of limit cycles, and due to its approximation nature, the results should be confirmed by time domain simulations. Higher feedback control gains h_s cause the polar plot to intersect with the negative inverse of the describing function at lower values. Hence a parametric study has been carried out to understand how the feedback gain h_s affects the point of intersection.

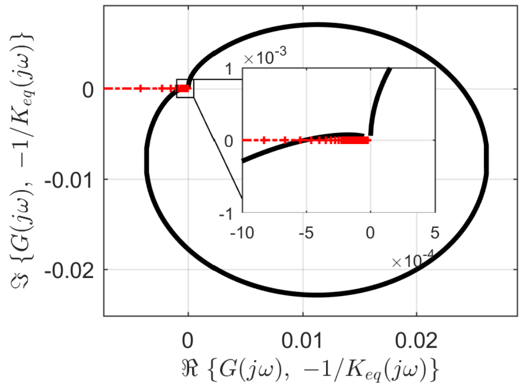

FIGURE 12: Polar plot of the underlying linear system FRF $G(j\omega)$ including VFC loop, and the negative inverse describing function $-1/K_{eq}(X_r)$ for the detection of limit cycles.

The amplitude of the limit cycle is shown in figure 13(a), which represents the maximum relative displacement reached by the proof mass. For low values of h_s, a higher relative displacement is needed to 'activate' the limit cycle when

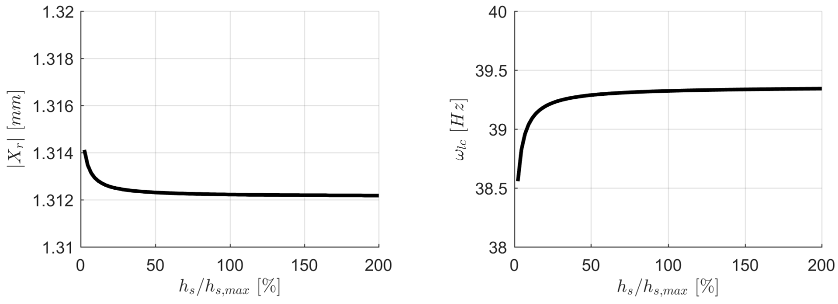

(a) (b)

FIGURE 13: Amplitude and frequency of the limit cycle oscillation for several values of the VFC gain h_s. (a) Amplitude; (b) Frequency.

compared to higher values of h_s. For high values of the feedback gain, the curve is almost flat and settled around 1.31 mm. Figure 13(b) shows the frequency of the limit cycle oscillations versus the feedback gain. The frequency of the limit cycle increases as the feedback gain increases, but also in this case for high values of h_s the curve is almost flat at around 39.3 Hz. These results can be verified by analysing time domain impulse response of the system for increasing feedback gains.

Figure 14 shows the time series of the proof mass, structure and relative displacements, respectively, due to an external impulse excitation of the type,

$$f_e = Pe^{-\left(\frac{t}{\tau}\right)^2}, \tag{51}$$

where $P = 10$ N is the initial amplitude of the impulse and $\tau = 1$ ms is the decaying rate of the impulse excitation. The dash-dotted red line of figure 14 shows the response of the uncontrolled system. As the feedback gain is increased to $25\% h_{s,max}$ (dotted blue line), the response of the structure to the same impulse is significantly reduced at the expense of the response of the proof mass. A further increase of the feedback gain to $40\% h_{s,max}$ (dashed green line) causes the relative displacement to overshoot the allowed stroke length, hence an impulse-like excitation is imparted to the structure, however, after

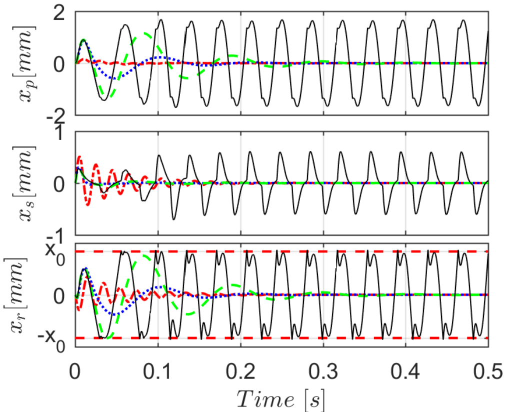

FIGURE 14: Response time histories of the closed-loop VFC system for increasing control gains using an impulse primary excitation on the structure and assuming a nonlinear model of the actuator. The uncontrolled system $h_s = 0$ is shown with the dash-dotted red line, $h_s = 25\% h_{s,max}$ with the dotted blue line, $h_s = 40\% h_{s,max}$ with the dashed green line, $h_s = 50\% h_{s,max}$ with the solid black line. The horizontal dashed red lines indicate the position of the stroke limits, which are considered in the nonlinear model of the actuator.

one impact the response decays away. Applying a slightly higher feedback gain $h_s = 50\% h_{s,max}$ (solid black line) results in an unstable system. It should be noted that the feedback gain causing the nonlinear system to become unstable is much lower than the one predicted by the linear Nyquist analysis for the underlying linear model of the system. The cause of this instability can be sought in the trajectories of the relative proof mass displacement in the phase-space for several feedback gains, which are shown in figure 15. It can be observed that an increase in the feedback gain rises the possibility of collisions with the end-stops, and for $h_s = 50\% h_{s,max}$ the proof mass experiences limit cycle oscillations. From the time simulation shown in figure14 and 15 the amplitude and frequency of the limit cycle oscillation can be derived. In fact, the maximum amplitude of the relative displacement results to be 1.29 mm, which is slightly lower than the one predicted by the describing function analysis. The frequency of the limit cycle can be calculated from the time series of figure 14 considering

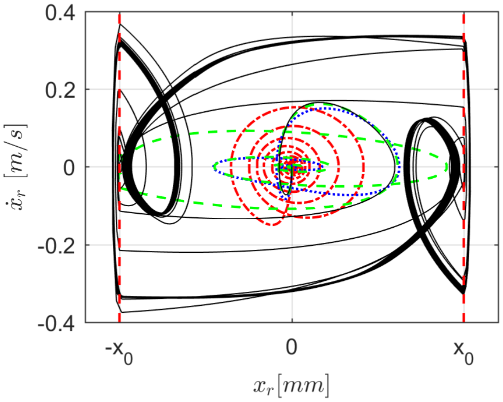

Figure 15: Response trajectories in the phase-space of the closed-loop VFC system for increasing control gains using an impulse primary excitation on the structure and assuming a nonlinear model of the actuator. The uncontrolled system $h_s = 0$ is shown with the dash-dotted red line, $h_s = 25\% h_{s,max}$ with the dotted blue line, $h_s = 40\% h_{s,max}$ with the dashed green line, $h_s = 50\% h_{s,max}$ with the solid black line. The vertical dashed red lines indicate the position of the stroke limits, which are considered in the nonlinear model of the actuator.

the zero crossing of the signal. It follows that the frequency of the limit cycle is 27.6 Hz, which is also lower than the one predicted by the describing function analysis. These discrepancies in the outcomes have to be attributed to the contribution of the higher harmonics in the response that the describing function tool does not take into account. However, the frequency of the limit cycle, hence, the frequency of the instability of the nonlinear system is higher than the frequency of the instability of the underlying linear system, which is about the resonance frequency of the actuator.

2.5. Nonlinear feedback control

The study of the previous section motivates for the development of a nonlinear controller, whose aim is to prevent the destabilisation of the VFC loop due to stroke saturation and to maintain the vibration attenuation performance provided by the VFC. In order to increase the stability of VFCs, in [10] the author proposed to use a combination of relative velocity feedback and absolute velocity feedback, where the tuning of the two feedback gains is a trade off between the stability and performance of the control system. Later on, other researchers dealt with the stroke saturation phenomenon using a NLFC, which is a function of the relative proof mass displacement [17]. This NLFC acts as a second loop alongside the VFC as shown in figure 2. In this section, the these two strategies are merged together to form a NLFC loop, whose control law is,

$$\psi(x_r, \dot{x}_r) = \frac{n_r \dot{x}_r}{(x_0 - |x_r|)^{2p} + b}, \tag{52}$$

hence a relative velocity feedback controller with a state dependent relative feedback gain that is given by,

$$\eta(x_r) = \frac{n_r}{(x_0 - |x_r|)^{2p} + b}, \tag{53}$$

where n_r is the feedback gain of the nonlinear controller, b is a limitation parameter and p is an exponent parameter. The control law of eq.(52) increases the active internal damping of the inertial actuator as the proof mass approaches the end-stops without adding any damping when the proof mass is close to the resting position. In fact, as the relative displacement of the proof mass gets close to the stroke limit, the denominator term of eq. (52) reduces, hence the current proportional to the relative velocity increases. The force applied to the structure by the NLFC can be written as,

$$f_{a,s,nlfc} = \phi \psi(x_r, \dot{x}_r), \tag{54}$$

thus, the active internal damping added to the actuator can be derived from eq.(54) and (52) as,

$$c_{a,nlfc}(x_r) = \frac{\phi \psi(x_r, \dot{x}_r)}{\dot{x}_r} = \frac{\phi n_r}{(x_0 - |x_r|)^{2p} + b}. \tag{55}$$

The control action can be bounded between a minimum active damping $c_{a,nlfc}(0) = c_{a,min}$, that is reached when the proof mass is centred within the casing, and a maximum active damping $c_{a,nlfc}(x_0) = c_{a,max}$ that is reached when the proof mass saturates in stroke. From this consideration, the parameters b and n_r can be calculated. Assuming $x_r = 0$ and $b \ll x_0$, the corresponding value of n_r can be calculated from eq.(55) as,

$$c_{a,min} = \frac{\phi n_r}{x_0^{2p}} \Rightarrow n_r = \frac{c_{a,min} x_0^{2p}}{\phi}. \tag{56}$$

Similarly, assuming $x_r = x_0$, the parameter b results,

$$c_{a,max} = \frac{\phi n_r}{b} \Rightarrow b = \frac{\phi n_r}{c_{a,max}}. \tag{57}$$

A graphical representation of the NLFC is shown in figure 16, where the dotted, dash-dotted and solid black lines represent the control action for the exponent parameters $p = 1, 2, 3$, respectively. The vertical dashed red lines, instead, represent the position of the stroke limits. It can be observed that increasing the exponent parameter p increases the active internal damping of the actuator on a bigger range of displacements. On one hand this can be beneficial for the stability of the system, but on the other hand it can be detrimental for the vibration attenuation performance when used in combination with the VFC.

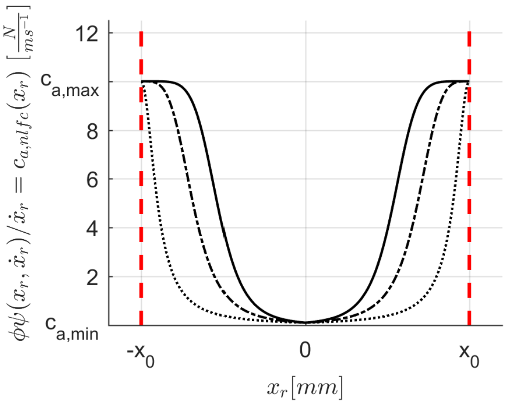

FIGURE 16: Nonlinear feedback control (NLFC) law for several exponent values. Dotted black line $p = 1$, dash-dotted black line $p = 2$, solid black line $p = 3$. The dashed red lines indicate the stroke limits of the inertial actuator.

In practice, the minimum and maximum active damping parameters given by eqs. (56,57) are selected using the internal damping ratio, which is defined as,

$$\zeta_a(x_r) = \frac{c_p + c_{a,nlfc}(x_r)}{2\sqrt{k_p m_p}} = \zeta_p + \frac{c_{a,nlfc}(x_r)}{c_c}, \tag{58}$$

where $c_c = 2\sqrt{k_p m_p}$ is the critical damping and $\zeta_p = c_p/c_c$ is the actuator's passive damping ratio. The internal damping ratio ζ_a should be chosen close to ζ_p for $x_r = 0$, this allows to maximise performance when stability is not an issue. In this study the internal damping ratio for small displacements is $\zeta_a(x_r = 0) = \zeta_p + 0.03$. On the other hand, the maximum internal damping ratio should be chosen to be larger than that of the critically damped system for $x_r = x_0$. In this study the maximum damping ratio has been chosen to be $\zeta_a(x_r = x_0) = 3$; this allows the actuator to become overdamped for displacements larger than 80% x_0 (considering $p = 1$) with a huge benefit for the stability. Of course, these parameters can be tuned to achieve other trade offs between stability and performance. The total internal damping ratio, given by the sum of passive and active damping, is shown in figure 17 as a function of the proof mass position within the actuator, where the dotted, dash-dotted and solid black lines represent the damping ratio for the exponent parameters $p = 1, 2, 3$, respectively. The vertical dashed red lines represent the position of the stroke limits, whereas the horizontal dash-dotted blue line shows the value of the passive damping ratio ζ_p.

The stability of the closed-loop system using the combination of VFC and NLFC can be analysed through the Lyapunov linearisation stability method [29] as shown for the single VFC loop. In fact, the VFC+NLFC closed-loop state dependent system matrix can be derived from eq.(23) as,

$$\mathbf{A}_{0,vfc+nlfc}(\mathbf{x}) = \left[\mathbf{A}(\mathbf{x}) - g_a \phi \mathbf{B}_a \mathbf{H}_{vfc+nlfc} \mathbf{C}\right]. \tag{59}$$

and the stability of the closed-loop VFC+NLFC system for several proof mass relative displacements and velocity feedback gains can be studied by analysing the real part of the largest eigenvalue of eq.(59). The real part of the maximum eigenvalue of $\mathbf{A}_{0,vfc+nlfc}$ for several proof mass displacements and velocity feedback gains is displayed in figure 18(a) and a detailed image around the stroke

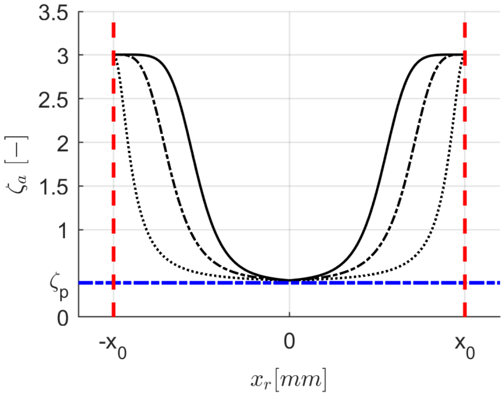

Figure 17: Internal damping ratio for several exponent values. Dotted black line $p = 1$, dash-dotted black line $p = 2$, solid black line $p = 3$. The dashed red lines indicate the stroke limits of the inertial actuator; the horizontal dash-dotted blue line shows the value of the passive damping ratio ζ_p.

limit region is shown in figure 18(b), where the stroke limits are represented with dashed red lines and the minimum and maximum active internal damping chosen for the calculation of the NLFC parameters are $c_{a,max} = 10$ N/ms^{-1} and $c_{a,min} = 0.1$ N/ms^{-1} and $p = 1$. A comparison between figure 18 and figure 10 shows that the NLFC enlarges the stability region of the system in terms of relative proof mass displacements. In fact, the delimiter of instability $\Re\{\lambda_{max}\left[\mathbf{A}_{0,vfc}(x_r, h_s)\right]\} = 0$ for the VFC+NLFC loop is shifted to larger relative displacements with respect to the one of single VFC loop. However, the dual loop controller becomes unstable if $h_s > h_{s,max}$ is chosen, because of the choice to use a small active internal damping for the proof mass around resting position. The NLFC can be sensitive to uncertainty in the estimation of the stroke length parameter. If the stroke length is underestimated, the NLFC law will add more damping than required, making the system stable, but at the expenses of some reduction of the vibration performance provided by the velocity feedback control (VFC) loop. If the stroke length is overestimated, the NLFC law will add less damping than required, making the system less stable, which means that for large amplitude excitations the stability of the system is not

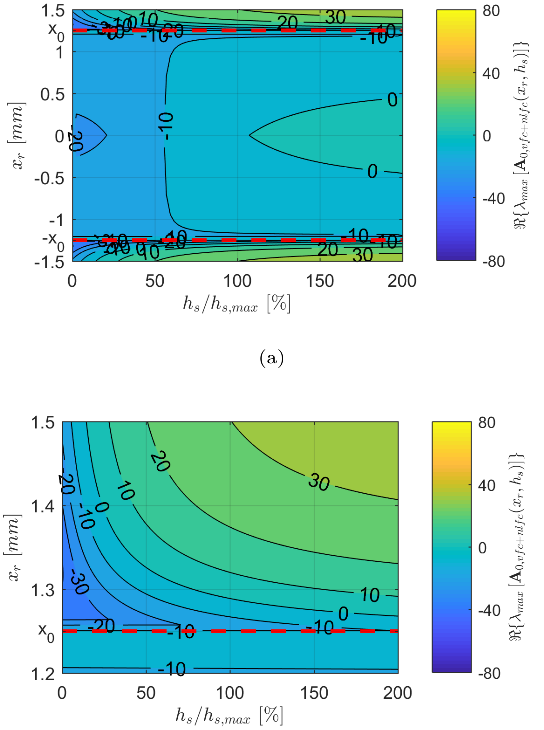

(a)

(b)

FIGURE 18: Real part of the maximum eigenvalue of the closed-loop matrix $\mathbf{A}_{0,vfc+nlfc}(\mathbf{x})$ for several values of the relative proof mass displacement x_r and velocity feedback gain h_s. (a) full range; (b) zoom into the stroke limit.

guaranteed. Hence, it is important to carefully estimate the stroke length and to use a marginally smaller value in the NLFC law to account for uncertainty. Time simulation studies are carried out to assess the performance of the NLFC. In particular, a comparison is made between the control system with single VFC loop and VFC+NLFC loop. Figure 19 shows the time history and the phase-space trajectory of the system for a feedback gain $h_s = 50\% h_{s,max}$ when controlled by a single VFC loop (dashed green line) and when it is controlled by a VFC+NLFC loop (solid black line) using an impulse excitation of the type given by eq.(51) . In this scenario the system goes unstable if the single VFC loop is used, whereas implementing the NLFC described by eq.(52) allows the proof mass to stand clear of the end-stops avoiding the limit cycle oscillation and hence the system remains stable. The stability of the nonlinear system does

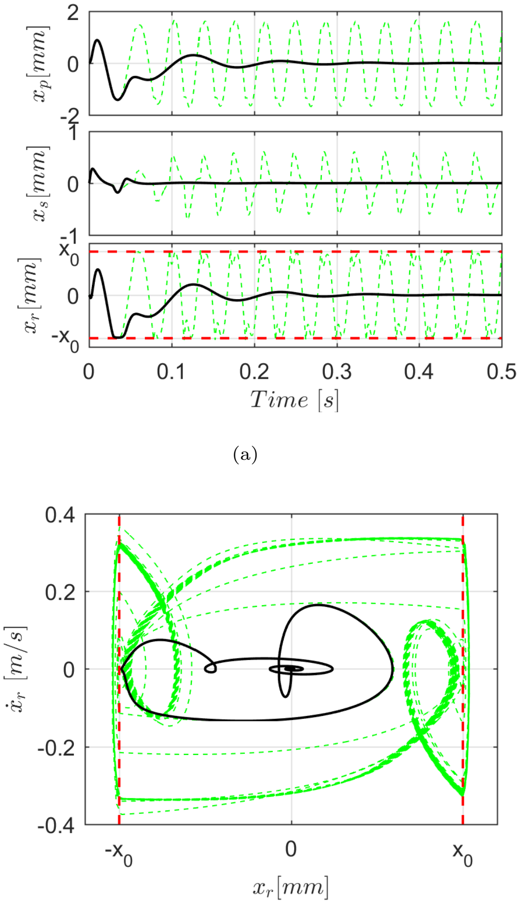

(a)

(b)

FIGURE 19: Response time histories and phase-space trajectories of the closed-loop VFC system (dashed green line) and the closed-loop VFC+NLFC system (solid black line) for a feedback gain $h_s = 50\% h_{s,max}$, using an impulse primary excitation on the structure and assuming a nonlinear model of the actuator. The dashed red lines indicate the position of the stroke limits. (a) Time history; (b) Phase-space trajectory.

not depend only on the value of the VFC gain h_s, but also on the magnitude of the impulse excitation P. Therefore, a parametric study has been carried out in order to investigate the potential benefits of the NLFC over different scenarios. In particular, the stability of the system has been evaluated for each possible value of P and h_s, and for the two testing conditions of single VFC loop or the combination of VFC and NLFC loops. For each scenario, the operating region $\mathcal{OR}(P, h_s)$ of the inertial actuator is defined as,

$$\mathcal{OR}(P, h_s) = \{(P, h_s)| \max_{t\to\infty} |x_r(t)| < x_0\}, \tag{60}$$

where the sets of (P, h_s) inside the operating region are those in which the system is stable and the inertial actuator is adding active damping to the structure. The results of the parametric study are shown in figure 20. The dark grey area delimited by the dotted black line shows the safe operating region when the single VFC loop is implemented. It can be seen that the nonlinearity in the inertial actuator severely reduces the stability of the system for large values of the excitation or the feedback gain. It should be noted that for very low values of excitation, the operating region reaches 100 % of $h_{s,max}$ because the proof mass does not reach the end-stops and the system behaves linearly. However, as soon as the excitation value is increased, the maximum gain that can be fed to the actuator without reaching the instability quickly drops down. Repeating the same parametric study, but using the combination of VFC+NLFC loops, produces a completely different result, which is shown in figure 20 with the light grey area delimited by the solid black line. In this case, the area covered by the operating region of the actuator using both VFC and NLFC loops is bigger than the area of the single VFC loop, hence, it increases the safe operating region of the inertial actuator. Moreover, the maximum gain that can be fed to the actuator slightly overshoots $h_{s,max}$, because, even for low excitations, the NLFC increases the effective internal damping of the actuator.

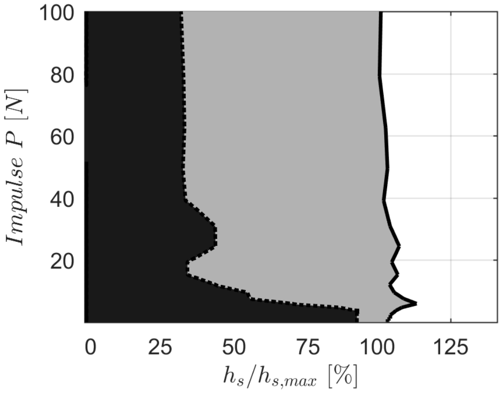

FIGURE 20: Operating regions of the inertial actuator for the closed-loop VFC system (dark grey area) and the closed-loop VFC+NLFC system (light grey area) for increasing values of the feedback gain, using an impulse primary excitation on the structure of amplitude P and assuming a nonlinear model of the actuator.

3. Nonlinear feedback control of a SDoF system: experimental analysis

The nonlinear feedback controller (NLFC) presented and studied using numerical simulations in 2 has been shown to increase the stability region of nonlinear inertial actuators. This section aims to investigate the experimental implementation of the NLFC and how it compares with the VFC in terms of stability of the closed-loop system under different scenarios. The author is not aware of experimental work on similar control strategies. In fact, the most similar nonlinear controller to the NLFC presented in this thesis can be found in [17, 18, 19, 20, 21], which has been analysed only by theoretical studies. Experimental implementation of controllers that account for stroke saturation can be found in [25, 32, 33, 34, 7, 23, 26], however, these controllers focus mainly on strategies that limit or reduce the VFC gain. The main objective of this study is to implement the NLFC law developed in the previous section on a stroke limited inertial actuator that is used to control the first mode of a cantilever beam. Firstly, the experimental set-up is presented in section 3.1, where the actuator is attached to the beam in a position where the structure's response is dominated by its first mode. The open-loop FRF of the VFC system is measured for a unit feedback gain and the underlying linear gain margin is calculated in section 3.2. The closed-loop response of the VFC to an impulsive primary excitation for several values of the feedback gain and levels of excitation has also been measured. Finally, the NLFC implementation is discussed in section 3.3 and the closed-loop response of the combined VFC+NLFC loop is compared with that of the single VFC loop in terms of the stability of the control system.

3.1. Experimental set-up and modal analysis

The experimental set-up is shown in figure 21. It consists of an aluminium cantilever beam and a control unit attached at the nodal point of the second mode of the beam, which is 38 mm away from the free end of the beam. The control unit consists of a stroke limited inertial actuator, a collocated accelerometer attached to the actuator casing and a force cell positioned between the beam and the proof mass actuator.

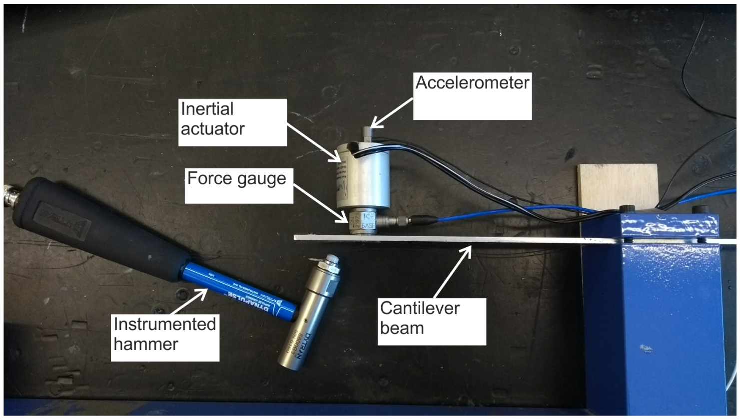

FIGURE 21: Experimental set-up for the active vibration control of the first mode of a cantilever beam using a stroke limited inertial actuator. The set-up consists of an aluminium cantilever beam, a force gauge, a stroke limited actuator and a collocated accelerometer. The excitation is given by an instrumented hammer. The control unit is attached to the nodal point of the second mode of the beam.

A modal analysis was performed prior to the active control experiment using LMS Test.Lab® and a SCADAS data acquisition system. The cantilever beam is excited by a Dytran (Dynapulse 5800B3 S/N 6160) roving hammer, which can be equipped with three different tips. A stiff aluminium tip (127-6250), a medium stiff Delrin tip (127-6250P) and a soft polyurethane tip (127-6250PS). Due to the light damping of the structure under testing, the Delrin plastic tip is used throughout the experiment. The response of the beam is measured by a B&K accelerometer (type 4375V) fixed on the free end. The acceleration signal passes through a B&K charge amplifier (type 2635) before being acquired by the SCADAS.

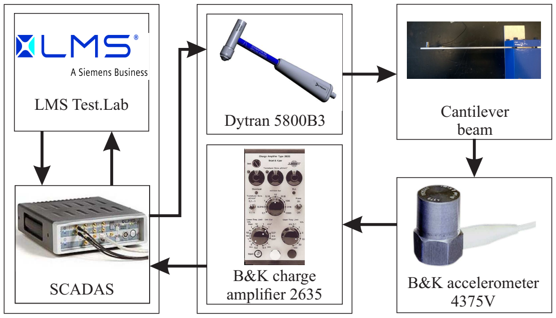

FIGURE 22: Block diagram of the modal analysis experimental set-up.

The test rig is shown in figure 23(a), which comprises of an aluminium bar with rectangular cross section, 25 mm width, 3 mm thick and 175 mm long and a a rigid connection to the ground at one end of the beam. The accelerometer is placed 7.5 mm away from the free end, which is shown in figure 23(b) as the point h_{11}. The hammering points are indicated with a progressive number starting from h_1 to h_{11} and they are spaced 15 mm apart, except for h_{10} and h_{11} that are 17.5 mm apart.

The experimental analysis is conducted by hammering 5 times at each point on the grid and taking the averaged FRF. An example driving point FRF (H_{11}) between acceleration and input force, both at position h_{11} is shown in figure 24 with the solid blue line and is compared with a theoretical model of the can-

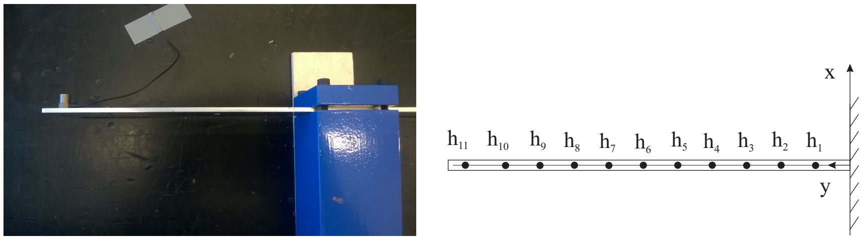

(a) (b)

FIGURE 23: Experimental test rig for the identification of the beam natural frequencies and mode shapes. (a) Picture of the test rig; (b) Sketch of the hammering point grid.

tilever beam shown with the solid red line [35]. The experimental results are in good agreement with the derived theoretical model. The first and second experimentally identified resonances are 68.5 Hz and 443.2 Hz, while the theoretical ones are 68.9 Hz and 458.8 Hz, respectively.

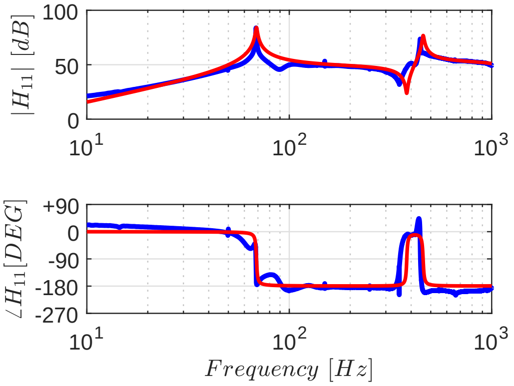

FIGURE 24: Comparison between the experimental and simulated FRFs of the beam at driving point h_{11}. The blue solid line shows the experimental FRF, whereas the red solid line displays the simulated FRF.

For frequencies below 1 kHz, the response of the beam is dominated by the first two modes. Using the toolbox provided by LMS Test.Lab® the mode shapes associated with the measured natural frequencies can be estimated. The

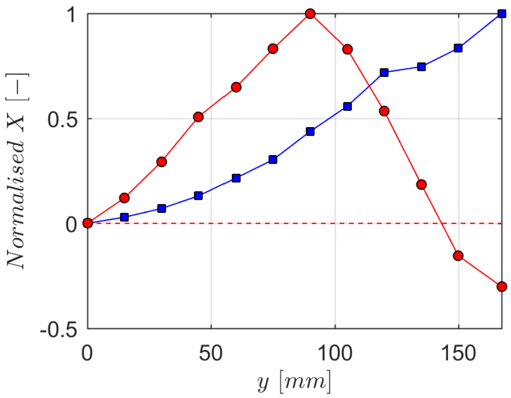

FIGURE 25: First and second mode shapes of the beam derived with LMS Test.Lab ® modal analysis software and normalise with respect to their maximum value. Mode one occurs at 68.5 Hz and is displayed by the blue squares. Mode two occurs at 443.2 Hz and is indicated by the red circles.

first two mode shapes of the beam are shown in figure 25, where the grid is composed of the eleven hammering points shown in figure 23(b). It can be seen in figure 25 that the first mode is characterised by an in phase motion of all the points along the beam, as expected. The second mode, however, has both in phase and out of phase motion, with a nodal point when the amplitude of this mode is zero. Any force applied to this point would affect only the first mode of the beam, hence, the control unit has been placed here in order that the response of the cantilever beam best approximates the response of a lumped parameter mass-spring model, as used in section 2.

Higher modes of the cantilever beam could be controlled by placing the control unit in a different location and/or adding more than one control unit. The control law would not need to be modified if controlling one or more modes, since it depends only on the actuator parameters and variables and it is independent of the hosting structure. The experiments have been conducted using the cantilever beam with zero initial conditions, with the excitation provided by an instrumented hammer, which ideally produces an impulse of force. Theoretically, impulse excitations can be seen as a sudden change in velocity [36], hence the study performed for different levels of input excitation can be seen also as for different values of initial velocity of the beam.

The parameters of the test rig are given in table 2 for the beam and in table 1 for the inertial actuator.

TABLE 2: Parameters of the cantilever beam and the control unit.

Property	Value	Units
l_{beam}	175	mm
b_{beam}	25	mm
h_{beam}	3	mm
m_{acc}	0.005	kg
m_{base}	0.053	kg
m_{gauge}	0.023	kg

3.2. Velocity feedback control of a cantilever beam

The inertial actuator is attached to the cantilever beam on the node of the second mode of the beam, as suggested by the analysis of the previous section. The test rig for the active vibration control of a beam using a stroke limited inertial actuator is shown in 21. The cantilever beam is excited on its free end by a Dytran (Dynapulse 5800B3 S/N 6160) hammer with a medium stiff Delrin tip (127-6250P). The signal of the primary force is acquired by a dSPACE 1103 PPC Controller Board, where the analogue-to digital conversion (ADC) is also performed with a sampling frequency f_s =10 kHz. The response of the beam at the control position is measured by a B&K accelerometer (type 4375V) fixed on the actuator casing connected to a B&K charge amplifier (type 2635), where the signal is integrated and high-pass filtered with a cut off frequency of 1 Hz. The force signal is measured by a PCB Piezotronics 208C01 ICP force sensor passing through a signal conditioner. All the measurements are then recorded by ControlDesk Next Generation software on a PC workstation. The control signal from the dSPACE passes through a low pass analogue filter with a cut-off frequency at 4 kHz before entering the Micromega Dynamics voltage driven current amplifier PR-052-01-04-03 and then the inertial actuator.

The same approach used in the theoretical study of section 2 has been applied for the experimental study. Firstly, the open-loop FRF has been measured for small excitation signals in order to obtain the underlying linear gain margin of the VFC. Consequently, the VFC closed-loop response has been measured for several excitation levels and velocity feedback gains. The open-loop control diagram is the one represented in figure 6, where $Y(s) = \dot{X}_c(s)$ is the response of the beam at the control position, $r(s)$ is the input reference signal from the dSPACE and the mobility transfer function $G_{sa}(s) = G_{cc}(s)$. The stability of the system is analysed using the Nyquist criterion for the open loop FRF $L(j\omega) = g_a h_s G_{cc}(j\omega)$. The control gain h_s is set to unity and the actuator is driven by a broadband white noise current. This results in the polar plot shown in figure 26. It can be seen that the locus of the Nyquist intersects the negative real axis at a distance δ =0.068, which corresponds to a gain margin $g_m = 1/\delta = 14.7$. As a result, the maximum VFC gain calculated with a linear stability analysis that can be applied to the system without driving it unstable is $h_{s,max} = 14.7$. The other visible circles on the right half plane of figure 26 correspond to the upper natural frequencies of the system.

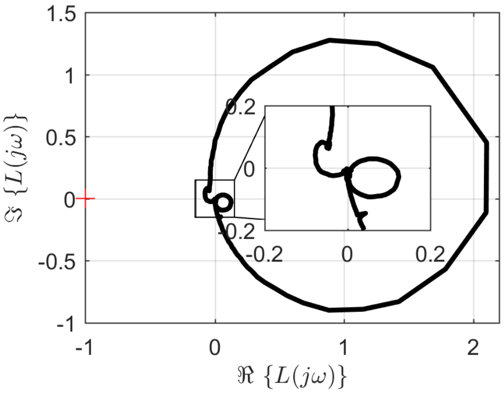

FIGURE 26: Nyquist plot of the measured open-loop FRF using a VFC gain $h_s = 1$.

The measured open-loop FRF with $h_s = 1$ is also shown in amplitude and phase in figure 27 with the black solid line. Figure 27 also shows that the measured open-loop FRF is well approximated by the simulated open-loop FRF of a SDoF lumped parameter model with the inertial actuator (blue dash-dot line).

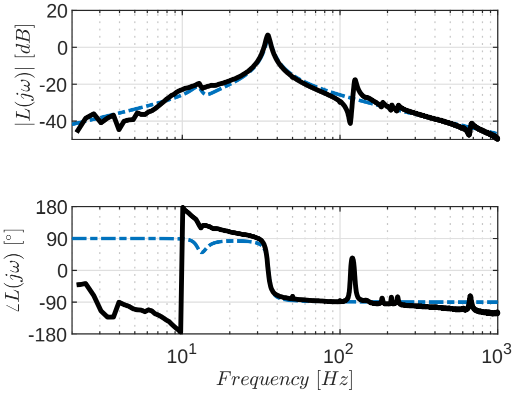

FIGURE 27: Bode plot of the measured open-loop FRF using a VFC gain $h_s = 1$ (black solid line) and simulated open-loop FRF of a SDoF lumped parameter model with the inertial actuator (blue dash-dot line).

After the stability has been assessed using the Nyquist criterion, the performance of the active control system is investigated evaluating the closed-loop FRFs. The closed-loop control diagram is the one represented in figure 8, where$F_e(s) = F_p(s)$ is the primary excitation at the tip of the beam, and $G_{se}(s) = G_{cp}(s)$ is the mobility at the control position due to a primary excitation at a different location. In this case the system is excited by an impulse at the free end of the beam using the instrumented hammer. A fixed control gain h_s is implemented for each test case, starting from the uncontrolled case and increasing its value until instability is reached. The data acquisition is performed using the ControlDesk software, where the trigger and pre-trigger settings are adjusted in order to record all the information of the signals and limiting the acquisition of the noise. Each acquisition is 5 seconds long and 5 acquisitions are preformed for each test case (same h_s), then the mean FRF is plotted. Both the excitation and response signals are windowed using classical windows for hammer testing. An exponential window has been applied to both the signals to improve the signal to noise ratio since the noise can take over the signal towards the end of the acquisition time, where the response has decayed away. This window has been applied to both the signals to account for the damping correction. An additional force window is applied to the force signal to eliminate noise on the force channel after the impact. In fact, this noise is not an input energy that excites the system being tested. The windowing functions adopted in this study can be found also in [37, 38]. The FRFs of the closed-loop response are then estimated using the H_1 estimator defined as the ratio between the cross-spectrum of the input and output signals and the auto-spectrum of the input signal [36], and averaged between all the measurements.

The results are shown in figure 28 for feedback gains h_s from 0 (passive system) marked with the solid black line, $6\% h_{s,max}$ marked with the dotted blue line, $12\% h_{s,max}$ marked with the dash-dotted green line, to $18\% h_{s,max}$ marked with the dashed red line. By increasing the control gain, the resonance peak of the first mode of the structure is effectively reduced, whereas the behaviour of the system at higher frequencies is not affected by the increase in the control gain. However, the vibration of the beam is significantly reduced as it is mainly determined by the first mode. A more detailed observation of figure 28 shows the presence of an increase of the response amplitude at a frequency around 12 Hz, which can be associated with the damping of the inertial actuator being reduced and consequently the resonance peak being increased.

As the feedback gain is further increased, collisions between the proof mass and the actuator casing are observed and the system is susceptible to become unstable. The instability not only depends on the value of the feedback gain, but also on the amount of energy that the initial impulse releases into the system. The FRFs of the closed-loop response for feedback gains also from $24\% h_{s,max}$ to $42\% h_{s,max}$ are presented in figure 29. For $h_s = 24\% h_{s,max}$, shown with the thin solid cyan line, a significant increase of the response for

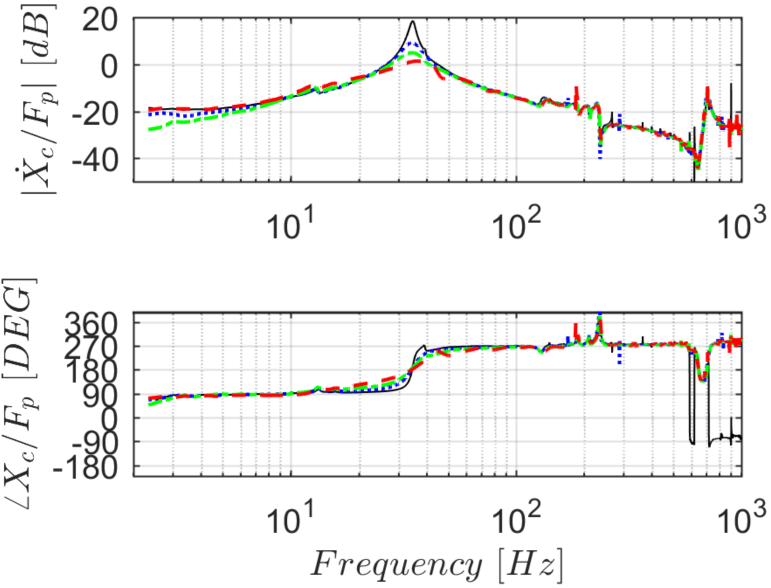

FIGURE 28: Bode plot of the measured closed-loop FRF with of the mobility at the control position for several VFC gains as follows. The solid black line shows the response of the uncontrolled beam, the dotted blue line shows the response for $h_s = 6\% h_{s,max}$, the dash-dotted green line shows the response for $h_s = 12\% h_{s,max}$ and the dashed red line shows the response for $h_s = 18\% h_{s,max}$. No stroke saturation has been observed for these cases.

frequencies below the structural resonance are observed. In fact, the proof mass is subject to some impact after the initial excitation, but after a finite time the response decays away. Increasing the feedback gain to $h_s = 30\% h_{s,max}$, several collisions reported after the initial impulse and also in this case the response decays away after a certain time. The FRF of the response for $h_s = 30\% h_{s,max}$ is displayed with the thin dotted blue line and shows a more noticeable spillover effect and also the presence of another peak at around 21 Hz. A larger increase in the feedback gain for example $h_s = 36\% h_{s,max}$ (thin dash-dotted green line) and $h_s = 42\% h_{s,max}$ (thin dashed red line), eventually leads the system to instability even for small amplitudes of initial excitation. The vibration is thus self-sustained due to the fact that the response does not decay away and the

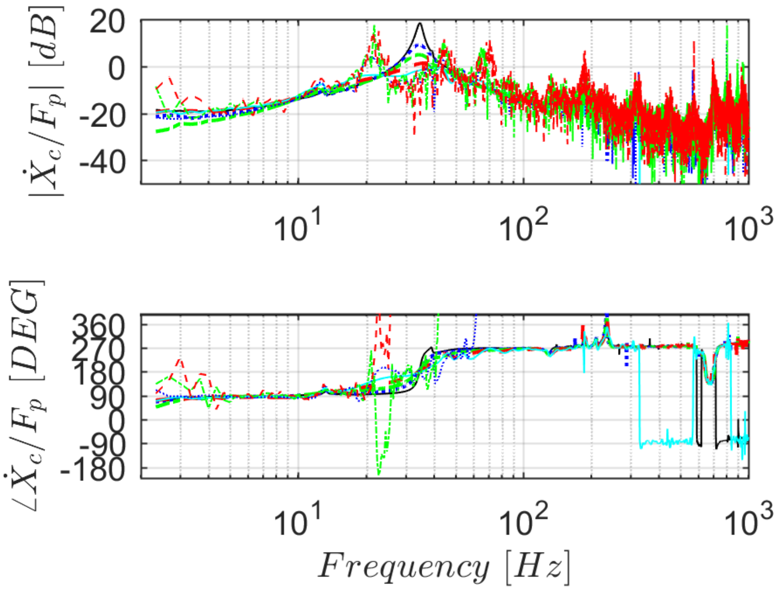

FIGURE 29: Bode plot of the measured closed-loop FRF with of the mobility at the control position for several VFC gains as indicated in the previous figure and as follows. The thin solid cyan line shows the response for $h_s = 24\% h_{s,max}$, the thin dotted blue line shows the response for $h_s = 30\% h_{s,max}$, the thin dash-dotted green line shows the response for $h_s = 36\% h_{s,max}$ and the thin dashed red line shows the response for $h_s = 42\% h_{s,max}$. Stroke saturation has been observed for $h_s > 24\% h_{s,max}$.

control system continues to insert power into the system. It can be seen that for these last two cases the peak at 21 Hz shoots up and also the response at frequencies higher than the first structural resonance shows a significant increase.

A comparison between the uncontrolled beam and the VFC of the beam has also been made in time domain and the results are shown in figure 30. This figure compares the response of the system for $h_s = 0$ (dashed red line) and $h_s = 42\% h_{s,max}$ (dash-dotted black line) under equal excitation levels. Figure 30(a) shows the spectrum of the excitation force and the time history of the velocity of the beam at the control point. Figure 30(b) shows, instead, the

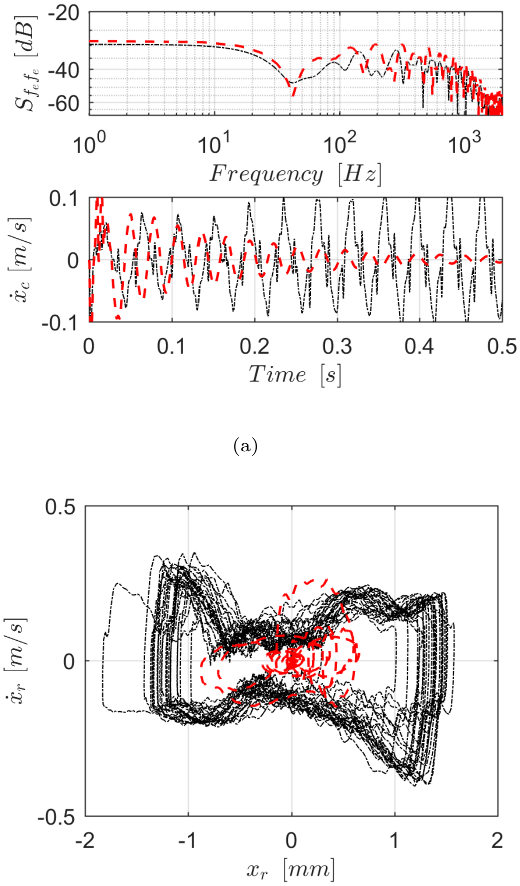

(a)

(b)

FIGURE 30: (a) Spectrum of the excitation force and time history of the velocity signal at the control point; (b) Phase-space trajectory of the relative proof mass displacement and velocity. Dashed red line for the uncontrolled scenario and dash-dotted black line for the single VFC scenario using $h_s = 42\% h_{s,max}$.

phase-space trajectory of the proof mass relative displacement and velocity. In the uncontrolled scenario, the vibration of the structure dies out after a certain period of time. Also, the trajectory of the proof mass starts to orbit around the equilibrium point until it eventually decays to zero. If the VFC with a feedback gain $h_s = 42\% h_{s,max}$ is implemented, the response of the system changes dramatically. In fact, the trajectory of the proof mass experiences limit cycle oscillations that are self-sustained and lead the VFC system to instability for the same level of excitation of the uncontrolled scenario. In the next section the NLFC loop is implemented in order to tackle this instability issue.

3.3. Nonlinear feedback control of a cantilever beam

The combined VFC+NLFC controller is then implemented as illustrated in the schematic of figure 31. The signal of the accelerometer at the control position is acquired by the dSPACE, it is then digitally high-pass filtered with a cut-on frequency of 2 Hz and integrated using the trapezoidal rule in order to obtain the velocity signal at the control position. The velocity of the structure is then multiplied by a VFC gain h_s and the amplified signal is then fed into the actuator through the amplifier. This forms the VFC loop. The NLFC loop, instead, has been designed according to eq.(52) to add a minimum internal damping of $c_{min} = 0.5$ N/ms^{-1}, a maximum internal damping of $c_{max} = 100$ N/ms^{-1} and an exponential coefficient $p = 1$. Using these values, all the parameters of the NLFC can be determined. For this control loop, both the force cell signal f_c and the acceleration signal $\ddot{x}_c$ have been filtered with a second order Butterworth high-pass filter with a cut-on frequency of 2 Hz.

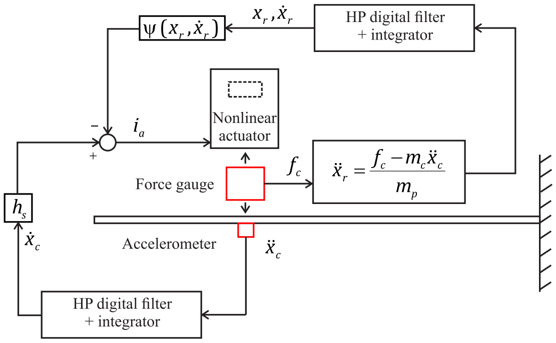

FIGURE 31: Schematic of the experimental implementation of the VFC and NLFC.

The proof mass relative acceleration has been calculated as,

$$\ddot{x}_r = \frac{f_c - m_c \ddot{x}_c}{m_p}, \tag{61}$$

where,

$$m_c = m_{acc} + m_b + m_{gauge}, \tag{62}$$

is the total mass attached to the beam at the control position, $m_{acc} = 0.005$ kg is the mass of the accelerometer and $m_{gauge} = 0.023$ kg is the mass of the force cell. The relative proof mass velocity and displacement are then estimated by high-pass filtering and integrating the acceleration signal, in the same way as it has been discussed for the structure's velocity signal. The NLFC control signal is then calculated in real time using eq.(52) before being fed back to the actuator.

Figure 32 shows a comparison of the response of the beam and proof mass among the uncontrolled scenario (dashed red line), the single VFC loop with $h_s = 42\% h_{s,max}$ (dash-dotted black line) and the combined VFC+NLFC loop with $h_s = 42\% h_{s,max}$ (blue solid line) under equal excitation levels. Figure 32(a) shows the spectrum of the excitation force and the time history of the velocity of the beam at the control point. Figure 32(b) shows, instead, the phase-space trajectory of the proof mass relative displacement and velocity. It can be observed that under the same excitation condition, the systems that implements the combined VFC+NLFC is able to avoid stroke saturation and hence the limit cycle oscillations of the proof mass so that the control system remains stable. In fact, the response of the beam quickly dies out and the trajectory of the proof mass goes to zero. The theoretical parametric study performed in section 2 has been repeated experimentally in order to test the robustness of the controller to increasing control gains and to increasing levels of excitation.

The beam has been excited with three different levels of excitation, namely: low (below 20 N peak amplitude, medium (between 20 N and 30 N) and high (above 30 N). For each level of excitation, the test has been repeated increasing the VFC gain from the uncontrolled scenario to $h_{s,max}$ with steps of $7\% h_{s,max}$.

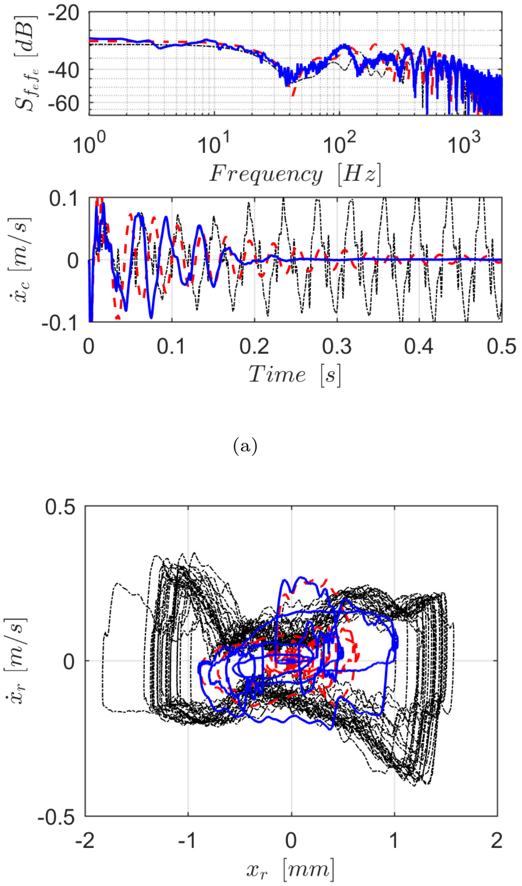

(a)

(b)

FIGURE 32: (a) Spectrum of the excitation force and time history of the velocity signal at the control point; (b) Phase-space trajectory of the relative proof mass displacement and velocity. Dashed red line for the uncontrolled scenario, dash-dotted black line for the single VFC scenario using $h_s = 42\% h_{s,max}$ and solid blue line for the VFC+NLFC scenario using $h_s = 42\% h_{s,max}$.

The parametric study has been conducted in the first place for the single VFC loop and then for the combined VFC+NLFC loop in order to compare the operating regions of the stroke limited actuator for the two different control strategies. The results are shown in 33, where the red circles are the experimental data points in which the single VFC loop is stable and the black asterisks are the experimental data points in which the combined VFC+NLFC is stable. Each point in figure 33 corresponds to an experiment of the same type of the one presented in figure 32. The data points of the two control strategies define the operating regions of the inertial actuator that are highlighted by the light grey area for the single VFC loop and by the dark grey area for the combined VFC+NLFC loop. It is clear that the added NLFC loop is able to extend the stability region of the inertial actuator to larger control gains and higher level of excitation compared to a single VFC loop.

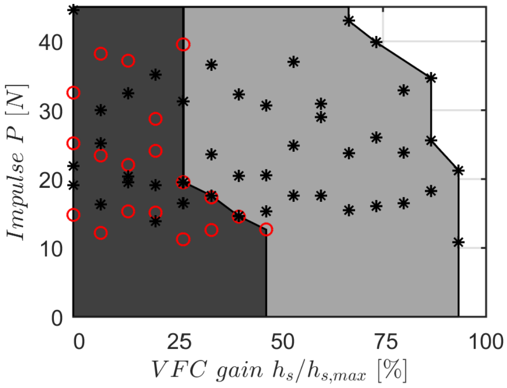

FIGURE 33: Comparison between the single VFC and VFC+NLFC in terms of stability range for the experimental investigation. The red circles in the dark grey area show the experimental data points in which the VFC is stable; the black asterisks in the light grey area show the experimental data point in which the combined VFC+NLFC controller is stable.

4. Conclusions

In this paper, a nonlinear feedback control strategy has been presented to avoid stroke saturation in inertial actuators. The paper is divided into a theoretical and an experimental part. Firstly, the mathematical model of a nonlinear inertial actuator connected to a single degree of freedom structure has been described, where the nonlinearity has been modelled by a bilinear stiffness. Secondly, simulation and analysis have shown that velocity feedback controllers are more liable to instability if the inertial actuator has stroke saturation nonlinearity. The impacts between the proof mass and the end stops then reduce the overall damping of the system, which results in instability for lower gains than those predicted by the linear analysis. This motivated the development of a nonlinear controller that operates as a second loop alongside the classical velocity feedback. This nonlinear controller increases the internal damping of the actuator as the proof mass approaches the end stops, being negligible when the proof mass is clear from the displacement constraints. A test rig consisting of a cantilever beam with a control unit attached to the free end has been used for the experimental investigation of the nonlinear controller. The real-time implementation of the nonlinear control law has been discussed and the results using VFC and VFC with NLFC have been compared, for several excitation levels and velocity feedback gains. In each test the stability of the system has been assessed. It has been shown both theoretically and experimentally that the nonlinear feedback controller is able to increase the safe operating region of the actuator. Hence, larger feedback gains can be used, or larger impulse excitations can be withstood, without the system becoming unstable if this nonlinear controller is used. Future work will be related on the estimation of the relative proof mass displacement in order to reduce the number of sensors and the added mass to the structure.

Acknowledgements

The authors gratefully acknowledge the European Commission for its support of the Marie Curie program through the ITN ANTARES project (GA 606817).

References

[1] C. C. Fuller, S. J. Elliott, P. A. Nelson, Active control of vibration, Academic Press, 1996.

[2] D. J. Inman, Vibration with control, John Wiley & Sons, 2006.

[3] A. Preumont, Vibration control of active structures: an introduction, Vol. 179, Springer, the Netherlands, 2011. `doi:10.1007/978-94-007-2033-6`.

[4] F. Fahy, P. Gardonio, Sound and structural vibration: radiation, transmission and response, 2nd Edition, Elsevier Science, 2007.

[5] Micromega Dynamics, Active damping devices and inertial actuators, last accessed: 2017-04-10.
URL `http://www.micromega-dynamics.com/download/category/4-active-damping-device.html`

[6] F. M. Ham, S. W. Greeley, B. L. Henniges, Active vibration suppression for the mast flight system, IEEE Control Systems Magazine 9 (1) (1989) 85–90. `doi:10.1109/37.16757`.

[7] I. Díaz, E. J. Hudson, E. Pereira, P. Reynolds, Experimental implementation of multi-actuator vibration control on an indoor walkway, in: 6th World Conference on Structural Control and Monitoring, Barcelona, Spain, 2014.

[8] Y. Ikeda, Active and semi-active vibration control of buildings in japan-practical applications and verification, Structural Control and Health Monitoring 16 (2009) 703–723. `doi:doi:10.1002/stc.315`.

[9] P. Gardonio, Review of active techniques for aerospace vibro-acoustic control, Journal of aircraft 39 (2) (2002) 206–214. `doi:10.2514/2.2934`.

[10] D. J. Inman, Control/structure interaction: effects of actuator dynamics, in: Dynamics Specialists Conference, Structures, Structural Dynamics, and

Materials, Long Beach, CA, USA, American Institute of Aeronautics and Astronautics, 1990, pp. 507–533. `doi:10.2514/6.1990-1223`.

[11] S. J. Elliott, M. Serrand, P. Gardonio, Feedback stability limits for active isolation systems with reactive and inertial actuators, Journal of Vibration and Acoustics-Transactions of the Asme 123 (2) (2001) 250–261. `doi:10.1115/1.1350822`.

[12] P. Gardonio, C. G. Díaz, Downscaling of proof mass electrodynamic actuators for decentralized velocity feedback control on a panel, Smart Materials and Structures 19 (2). `doi:10.1088/0964-1726/19/2/025004`.

[13] O. N. Baumann, S. J. Elliott, Destabilization of velocity feedback controllers with stroke limited inertial actuators, The Journal of the Acoustical Society of America 121 (5) (2007) EL211–EL217. `doi:10.1121/1.2731018`.

[14] O. N. Baumann, S. J. Elliott, The stability of decentralized multichannel velocity feedback controllers using inertial actuators, The Journal of the Acoustical Society of America 121 (1) (2007) 188–196. `doi:10.1121/1.2400674`.

[15] M. Dal Borgo, M. Ghandchi Tehrani, S. J. Elliott, Identification and analysis of nonlinear dynamics of inertial actuators, Mechanical Systems and Signal Processing 115 (2019) 338–360, https://doi.org/10.1016/j.ymssp.2018.05.044. `doi:https://doi.org/10.1016/j.ymssp.2018.05.044`.

[16] H. Politansky, W. D. Pilkey, Suboptimal feedback vibration control of a beam with a proof-mass actuator, Journal of Guidance Control and Dynamics 12 (5) (1989) 691–697. `doi:10.2514/3.20463`.

[17] G. A. Zvonar, D. K. Lindner, D. Borojevic, Nonlinear control of a proof-mass actuator to prevent stroke saturation, in: Dynamics and control of large structures; Proceedings of the 8th VPI & SU Symposium, Blacksburg, VA, USA, 1991, pp. 37–48.

[18] D. K. Lindner, T. P. Celano, E. N. Ide, Vibration suppression using a proofmass actuator operating in stroke/force saturation, Journal of Vibration and Acoustics-Transactions of the Asme 113 (4) (1991) 423–433. `doi:10.1115/1.2930203`.

[19] D. K. Lindner, G. A. Zvonar, D. Borojevic, Limit cycle analysis of a nonlinear controller for a proof-mass actuator, in: AIAA Dynamics Specialists Conference, Dallas, TX, USA, American Institute of Aeronautics and Astronautics, 1992, pp. 585–594. `doi:10.2514/6.1992-2140`.

[20] D. K. Lindner, G. A. Zvonar, D. Borojevic, Performance and control of proof-mass actuators accounting for stroke saturation, Journal of Guidance Control and Dynamics 17 (5) (1994) 1103–1108. `doi:10.2514/3.21316`.

[21] D. K. Lindner, G. A. Zvonar, D. Borojevic, Nonlinear control of a proof-mass actuator, Journal of Guidance, Control, and Dynamics 20 (3) (1997) 464–470. `doi:10.2514/2.4098`.

[22] L. I. Wilmshurst, M. Ghandchi Tehrani, S. J. Elliott, Preventing of stroke saturation in inertial actuators using a detection scheme, in: The 21st International Congress on Sound and Vibration (ICSV21), Beijing, China, 2014.

[23] L. I. Wilmshurst, M. Ghandchi Tehrani, S. J. Elliott, Active control and stability analysis of flexible structures using nonlinear proof-mass actuators, in: IX International Conference on Structural Dynamics (Eurodyn 2014), Porto, Portugal, 2014, pp. 1571–1578.

[24] E. G. Gilbert, K. T. Tan, Linear systems with state and control constraints: the theory and application of maximal output admissible sets, Ieee Transactions on Automatic Control 36 (9) (1991) 1008–1020. `doi:10.1109/9.83532`.

[25] D. Nyawako, P. Reynolds, Response-dependent velocity feedback control for

mitigation of human-induced floor vibrations, Smart Materials and Structures 18 (7) (2009) 14. `doi:10.1088/0964-1726/18/7/075002`.

[26] J. Rohlfing, T. May, L. Walter, J. Millitzer, Self-tuning velocity feedback control for a time varying structure using a voltage driven electrodynamic inertial mass actuator, in: 27th International Conference on Noise and Vibration Engineering (ISMA2016), Leuven, Belgium, 2016.

[27] M. Ahmadi, W. K. Ao, P. Reynolds, Prevention of stroke saturation of inertial actuators used for active vibration control of floor structures, in: The 7th World Conference on Structural Control and Monitoring, Qingdao, China, 2018.

[28] V. M. Ryaboy, Current developments in practical active damping systems for vibration-isolated platforms, The Journal of the Acoustical Society of America 134 (5) (2013) 4191–4191. `doi:10.1121/1.4831371`.
URL `https://asa.scitation.org/doi/abs/10.1121/1.4831371`

[29] J.-J. E. Slotine, W. Li, Applied nonlinear control, Prentice-Hall, Englewood Cliffs, NJ, USA, 1991.

[30] L. Arnold, V. Wihstutz, Lyapunov exponents: A survey, Vol. vol 1186 of Lecture Notes in Mathematics, Springer Berlin, Heidelberg, Berlin, Heidelberg, 1986, 10.1007/BFb0076830. `doi:https://doi.org/10.1007/BFb0076830`.

[31] H. K. Khalil, Nonlinear systems, 3rd Edition, Prentice-Hall, New Jersey, USA, 2002.

[32] I. M. Díaz, P. Reynolds, Robust saturated control of human-induced floor vibrations via a proof-mass actuator, Smart Materials and Structures 18 (12) (2009) 125024. `doi:10.1088/0964-1726/18/12/125024`.

[33] I. M. Díaz, P. Reynolds, On-off nonlinear active control of floor vibrations, Mechanical Systems and Signal Processing 24 (6) (2010) 1711–1726. `doi:10.1016/j.ymssp.2010.02.011`.

[34] I. M. Díaz, E. Pereira, P. Reynolds, Integral resonant control scheme for cancelling human-induced vibrations in light-weight pedestrian structures, Structural Control and Health Monitoring 19 (1) (2012) 55–69. `doi:10.1002/stc.423`.

[35] M. Dal Borgo, Active vibration control using a nonlinear inertial actuator, Institute of Sound and Vibration Research, University of Southampton, PhD thesis (2019).

[36] K. Shin, J. Hammond, Fundamentals of signal processing for sound and vibration engineers, John Wiley & Sons, 2008.

[37] D. L. Brown, R. J. Allemang, A. W. Phillips, Forty years of use and abuse of impact testing: a practical guide to making good frf measurements, in: Proceedings of the 33rd IMAC, A Conference and Exposition on Structural Dynamics, Orlando, FL, USA, 2015, pp. 221–241.

[38] W. G. Halvorsen, D. L. Brown, Impulse technique for structural frequency response testing, Sound and Vibration 11 (11) (1977) 8–21.